



# Duplex equilibria of Ural circulation anomalies

Dongdong Li<sup>1</sup> · Yongli He<sup>1</sup> · Jianping Huang<sup>1</sup>

Received: 23 January 2019 / Accepted: 21 November 2019  
© Springer-Verlag GmbH Germany, part of Springer Nature 2019

## Abstract

Atmospheric circulation anomalies over the Ural Mountains are crucial indicators of the anomalous downstream weather and climate over East Asia. Here, we provide a new perspective on the mechanism of Ural circulation anomalies. We use a simple theoretical model to determine that the relationship between the solar forcing and three Ural circulation patterns, namely, neutral type, trough anomaly and ridge anomaly, is a nonlinear relationship following the supercritical pitchfork bifurcation theory. The theory predicts that when the total solar irradiance (TSI) is below a critical value, trough and ridge anomalies represent duplex equilibria and are equally likely to occur at the same TSI. Based on 180 winter months record, we have estimated the bidimensional probability density of TSI and the monthly mean geopotential height at 500 hPa or zonal wind at 850 hPa over the Ural Mountains. Results show that  $S_c = 1360.9 \text{ W m}^{-2}$  is a critical value of TSI, the neutral type pattern is the single circulation regime when  $\text{TSI} > S_c$ , whereas trough and ridge anomaly patterns are duplex circulation regimes when  $\text{TSI} < S_c$ . Besides, when  $\text{TSI} < S_c$ , during the same TSI range, trough and ridge anomaly events occur at nearly the same frequencies. These results generally agree with the theoretical model. We demonstrate that trough and ridge anomalies, as duplex equilibria, result from the large-scale zonal flow interacting with the Ural Mountains. Low TSI tends to strengthen the large-scale zonal flow over the Ural Mountains, hence inducing either a trough anomaly or ridge anomaly.

**Keywords** Atmospheric circulation anomalies · Ural Mountains · Total solar irradiance (TSI) · Supercritical pitchfork bifurcation · Probability density function (PDF)

## 1 Introduction

The Ural Mountains extend roughly from north to south along 60° E through western Russia (Fig. 1), from the Arctic coast (ca. 70° N) to the northwestern Kazakhstan (ca. 50° N). The Ural region, as well as the North Atlantic and North Pacific, is one of the major regions for the recurrence of persistent atmospheric circulation anomalies over the Northern Hemisphere (Dole and Gordon 1983; Li and Ji 1994, 2001). In winter, an anomalous persistent ridge or blocking high over the Ural Mountains enhances cold air advection downstream from high latitudes, strengthening

the Siberian High and East Asian winter monsoon, hence enhancing cold conditions over East Asia (Tao 1957; Yeh et al. 1962; Ding 1994; Takaya and Nakamura 2005; Wang and Lu 2017; Yao et al. 2017). By contrast, increasing persistent troughs and decreasing blocking highs over the Ural Mountains facilitate the weaker Siberian High and East Asian winter monsoon, thus promoting warmer winters over East Asia (Wang et al. 2010; Cheung et al. 2012; Wang and Chen 2014). Atmospheric circulation anomalies over the Ural Mountains are crucial indicators of the anomalous downstream weather and climate over East Asia (Yeh et al. 1962; Ding and Chan 2005; Cheung and Zhou 2016; Tan et al. 2017). Therefore, understanding the mechanisms of atmospheric circulation anomalies over the Ural Mountains will help to improve the reliability of weather and short-term climate prediction over East Asia.

The Ural circulation anomalies have been attributed to many forcing factors, such as North Atlantic sea surface temperature (Palmer and Sun 1985; Li 2004; Han et al. 2011; Chen et al. 2018), Eurasian snow cover (Liu and Yanai 2002; Xu et al. 2017; Han and Sun 2018), Arctic

---

**Electronic supplementary material** The online version of this article (<https://doi.org/10.1007/s00382-019-05064-w>) contains supplementary material, which is available to authorized users.

---

✉ Jianping Huang  
hp@lzu.edu.cn

<sup>1</sup> Key Laboratory for Semi-Arid Climate Change of the Ministry of Education, College of Atmospheric Sciences, Lanzhou University, Lanzhou 730000, China

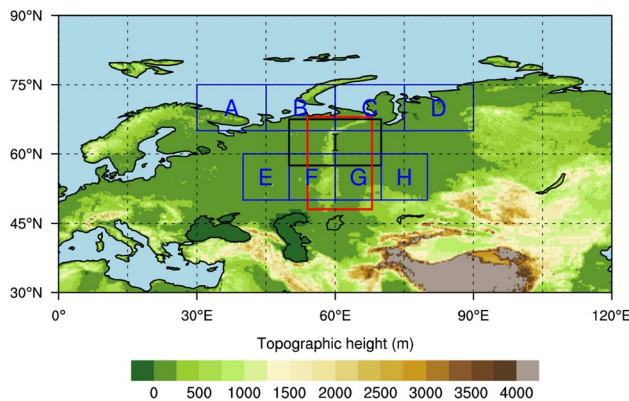


**Fig. 1** Topographic map of the Eurasia at mid-high latitudes, the red box ( $48^{\circ}$ – $68^{\circ}$  N,  $54^{\circ}$ – $68^{\circ}$  E) encloses the region of Ural Mountains. The blue boxes enclose eight regions: Region A ( $65^{\circ}$ – $75^{\circ}$  N,  $30^{\circ}$ – $45^{\circ}$  E), Region B ( $65^{\circ}$ – $75^{\circ}$  N,  $45^{\circ}$ – $60^{\circ}$  E), Region C ( $65^{\circ}$ – $75^{\circ}$  N,  $60^{\circ}$ – $75^{\circ}$  E), Region D ( $65^{\circ}$ – $75^{\circ}$  N,  $75^{\circ}$ – $90^{\circ}$  E), Region E ( $50^{\circ}$ – $60^{\circ}$  N,  $40^{\circ}$ – $50^{\circ}$  E), Region F ( $50^{\circ}$ – $60^{\circ}$  N,  $50^{\circ}$ – $60^{\circ}$  E), Region G ( $50^{\circ}$ – $60^{\circ}$  N,  $60^{\circ}$ – $70^{\circ}$  E), Region H ( $50^{\circ}$ – $60^{\circ}$  N,  $70^{\circ}$ – $80^{\circ}$  E), the black box encloses the Region I ( $57.5^{\circ}$ – $67.5^{\circ}$  N,  $50^{\circ}$ – $70^{\circ}$  E)

sea ice (Wu et al. 1999; Mori et al. 2014; Sun et al. 2016; Zhang et al. 2018), and the Tibetan plateau (Zheng et al. 1993; Yun et al. 2016). These forcing factors partially explain the Ural circulation anomalies. However, in the majority of previous studies, the positive and negative atmospheric circulation anomalies over the Ural Mountains were always regarded as different atmospheric responses to different forcing factors. It implies that most people subconsciously assumed a one-to-one relationship between a forcing factor and the atmospheric circulation anomalies. Different from most previous studies, in this paper, we find that the positive and negative circulation anomalies over the Ural Mountains can be considered duplex equilibria induced by the same solar forcing. That is, we consider a one-to-two relationship between solar forcing (an external forcing factor) and the positive and negative circulation anomalies over the Ural Mountains. Thus, our viewpoint seems to be novel.

The atmospheric circulation is driven by the thermal contrast due to the uneven incoming solar radiation at the Earth's surface. Numerous previous studies have examined the impacts of solar activity, particularly that of 11-year solar cycle on tropospheric circulation, such as the Northern and Southern Annular Modes (Ruzmaikin and Feynman 2002; Kuroda and Kodera 2005; Lee and Hameed 2007), North Atlantic Oscillation (Kodera 2003; Ogi et al. 2003; Ineson et al. 2011), atmospheric blocking (Barriopedro et al. 2008; Gray et al. 2016), and weather types (Huth et al. 2008; Schwander et al. 2017). Most of these studies consider a one-to-one relationship between the solar forcing and the atmospheric circulation anomalies. Different from these previous studies, we find that to some extent, the solar activity

inducing the positive and negative circulation anomalies over the Ural Mountains follows a one-to-two relationship.

Our work arises from a simple theoretical model associated with the supercritical pitchfork bifurcation theory proposed in our previous paper (Li et al. 2018; hereafter L18). The theoretical model suggests that the same solar radiation and topographic forcing may yield two types of stationary equilibrium states with opposite wave phase in the atmosphere flows. We find there is some similarity between the model atmospheric flow and the atmospheric circulation anomalies over the Ural Mountains. Guided by the theoretical model, we have examined the nonlinear relationship between the TSI and the Ural circulation anomalies. The results suggest that when TSI is less than a critical value, the positive and negative circulation anomalies over the Ural Mountains indeed can be considered duplex equilibria at the same TSI, and they should be equally likely to occur at the same TSI. To some degree, the relationship between TSI and Ural circulation anomalies is a one-to-two relationship following the simple theoretical model. The “supercritical pitchfork bifurcation theory” accounts for about 50% strong circulation anomalies events over the Ural Mountains in boreal winter. This study appears to provide a new perspective on the mechanism of solar influence on the atmospheric circulation anomalies over the Ural Mountains.

The paper is organized as follows. In Sect. 2, we describe the data and methods used in this study. In Sect. 3, we define the classification of Ural circulation patterns. In Sect. 4, we explain the theoretical model and describe the similarity between the model atmospheric flow and the atmospheric circulation anomalies over the Ural Mountains. In Sect. 5, to examine the extent to which the behavior of Ural circulation anomalies agrees with the theoretical model, the statistical properties of Ural atmospheric circulation during winter 1958–2017 are presented, the nonlinear relationship between TSI and Ural circulation anomalies is revealed. The physical mechanism that how does the solar activity induce the atmospheric circulation anomalies over the Ural Mountains is explored in Sect. 6. The discussion and conclusions are presented in Sects. 7 and 8, respectively.

## 2 Data and methods

The data used in this study includes the monthly mean geopotential height (GPH), sea level pressure, wind fields (zonal wind and meridional wind) and air temperature derived from the NECP-NCAR reanalysis 1, which covers 1948/01 to present (Kalnay et al. 1996). For comparison, the Japanese 55 year reanalysis (JRA-55) which covers 1958/01 to present (Kobayashi et al. 2015) is also used. The horizontal resolution of these data are  $2.5^{\circ}$  latitude  $\times 2.5^{\circ}$  longitude. The total solar irradiance (TSI) is the total electromagnetic

power per unit area of cross section arriving at the mean distance of the Earth from the Sun, and it shows a clear 11-year solar cycle variation between sunspot minimum and sunspot maximum (Fröhlich 2006; Gray et al. 2010). The monthly measured TSI time series which covers 1978/11 to present (Fröhlich 2006), the monthly reconstructed TSI time series which covers 1880/01 to present (Coddington and Lean 2015), were both downloaded from the Climate Explorer (<http://climexp.knmi.nl>). The measured TSI time series does not cover the time period before 1978/11, so only the results of reconstructed TSI time series are presented in the main body of this paper. The comparisons between measured and reconstructed TSI time series are discussed in Sect. 7.2. The monthly sea ice concentration on a 1.0 latitude–longitude grid is derived from the Met Office Hadley Center’s sea ice and sea surface temperature data set (HadISST1), which covers 1870/01 to present (Rayner et al. 2003). The monthly Northern Hemisphere Annular Mode index or Arctic Oscillation index is defined as the difference in the normalized monthly zonal mean sea level pressure between 35° and 65° N (Li and Wang 2003), it is calculated by using NECP–NCAR reanalysis 1 sea level pressure dataset, and it was downloaded at the website (<http://ljp.gcess.cn/dct/page/65607>).

To determine the multiple flow regimes in the observations, examining the multimodality (the presence of multiple peaks) in the probability density function (PDF) of a circulation index is a direct method (Hansen and Sutera 1986; Christiansen 2005; Hannachi et al. 2017). In this study, we calculate the PDF by using a MATLAB function named “ksdensity” (<https://ww2.mathworks.cn/help/stats/ksdensity.html>), it calculates the probability density for univariate and bivariate data based on a normal kernel function, and it returns the smoothed probability density estimate based on the default or specified bandwidth of the kernel smoothing window. We specify different bandwidths of the smoothing window for different variates in this study.

The upper bound on the number of the bins for histograms can be determined by the following formula (Emerson and Hoaglin 1983):

$$L = \lceil 10 \log_{10} n \rceil, \quad (1)$$

where  $\lceil x \rceil$  is the largest integer not exceeding  $x$ ,  $n$  is the sample size. When the upper bound on the number of the bins is obtained, the corresponding bin width for histograms and the bandwidth of the smoothing window for the PDF can be determined.

Student’s  $t$  test is used to estimate the statistically significance of a correlation for pairs of time series. However, time series of meteorological variables typically have nonzero autocorrelation, leading to the lack of independence of observations (Wilks 2011). One convenient method to

deal with this problem is to use an effective sample size,  $n'$ , to substitute the sample size,  $n$ . For two time series  $X = \{x_1, \dots, x_n\}$  and  $Y = \{y_1, \dots, y_n\}$ , the effective sample size for the correlation can be estimated by the formula (e.g., Afyouni et al. 2019; Pyper and Peterman 1998):

$$n' = n \left( 1 + 2 \sum_{k=1}^{n-1} \left( 1 - \frac{k}{n} \right) \rho_{XX,k} \rho_{YY,k} \right)^{-1}, \quad (2)$$

where  $\rho_{XX,k}$  and  $\rho_{YY,k}$  are the autocorrelation coefficients of X and Y at lag  $k$ , respectively. And  $\rho_{XX,k}$  is given by (Wilks 2011)

$$\rho_{XX,k} = \frac{\sum_{i=1}^{n-k} [(x_i - \bar{x}_-) (x_{i+k} - \bar{x}_+)]}{\sqrt{\sum_{i=1}^{n-k} (x_i - \bar{x}_-)^2} \sqrt{\sum_{i=k+1}^n (x_i - \bar{x}_+)^2}}, \quad (3)$$

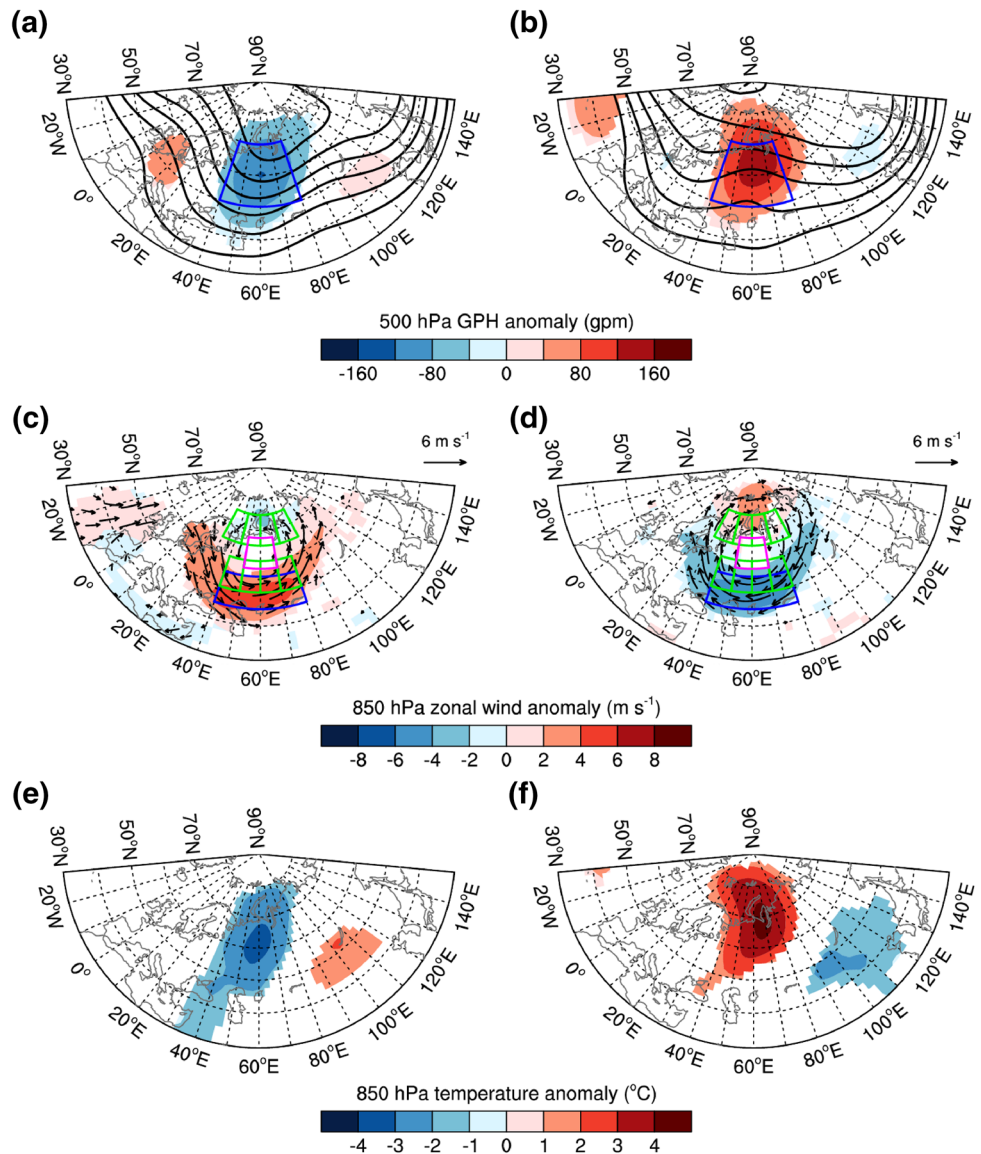
where the subscripts “–” and “+” indicate sample means over the first and last  $n-k$  data values, respectively. When using Eq. (2) to calculate the effective sample size,  $n'$ , we only consider the first  $\frac{n}{5}$  lags (Afyouni et al. 2019; Pyper and Peterman 1998).

### 3 Classification of Ural circulation patterns

To quantitatively classify the monthly mean atmosphere circulation patterns over the Ural Mountains, we define two circulation indices. The Z index is defined as the area-averaged GPH at 500 hPa over the domain (50°–70° N, 40°–80° E, see blue boxes in Fig. 2a, b). The U index is defined as the area-averaged zonal wind at 850 hPa over the domain (45°–55° N, 40°–80° E, see blue boxes in Fig. 2c, d). In the statistical analyses, we focus on winter months (December, January and February) of 60 years from 1958 to 2017. Thus, the sample sizes for the Z index and U index are both 180.

In this paper, we classify the Ural circulation patterns into 3 main categories (neutral type, trough anomaly, ridge anomaly) and 5 subcategories (neutral type, strong and weak trough anomaly, strong and weak ridge anomaly) based on the Z index and U index. For the 180 samples of Z index (mean 5307.52 gpm, standard deviation 60.17 gpm), if a Z index lies inside the 99% confidence interval of the mean value (5307.52 gpm), it is a neutral type event. The 99% confidence interval of the mean value is  $[Me - 2.576 \frac{Std}{\sqrt{n}}, Me + 2.576 \frac{Std}{\sqrt{n}}]$ , where  $Me$  represents the mean value,  $Std$  represents the standard deviation,  $n$  is the sample size. Because  $n=180$ , the 99% confidence interval of the mean value is  $[Me - 0.2Std, Me + 0.2Std]$ . Thus, in other word, if the absolute value of the negative or positive anomaly for a Z index is less than or equal to the 0.2 standard deviation, it is a neutral type event (Here the “anomaly” indicates that the mean value is subtracted). Whereas, if the

**Fig. 2** Composites of the monthly mean; **a, b** GPH (contours) and GPH anomaly (shaded) at 500 hPa; **c, d** horizontal wind (vectors) and zonal wind anomaly (shaded) at 850 hPa and **e, f** temperature anomaly at 850 hPa (shaded) for strong trough anomaly events (left panels) and strong ridge anomaly events (right panels), respectively. The “anomaly” indicates the deviation from the mean of 180 samples derived from winter 1958–2017 (i.e., the climatological mean). The contour intervals are 100 gpm and the ranges are 5100–5600 gpm in **a, b**. The shaded areas also denote the region above the 99% confidence level for two-sided Student’s *t* test. Wind vectors are plotted if they are significant in at least one direction (zonal or meridional). The eight green boxes in **c, d** are the same as the eight blue boxes in Fig. 1, the magenta boxes in **c, d** are the same as the black boxes in Fig. 1



absolute value of the negative (positive) anomaly for a Z index is greater than the 0.2 standard deviation, it is a trough (ridge) anomaly event. The 0.2 standard deviation is the default classification criterion for the neutral type and circulation anomalies events. The 0.4 and 0.6 standard deviations are also used for comparison.

In addition, if the absolute value of the negative (positive) anomaly for a Z index is greater than the 0.2 standard deviation but less than the 1.0 standard deviation (60.17 gpm), it is a weak trough (ridge) anomaly event. If the absolute value of the negative (positive) anomaly for a Z index is greater than or equal to the 1.0 standard deviation, it is a strong trough (ridge) anomaly event.

For the 180 samples of U index (mean  $3.98 \text{ m s}^{-1}$ , standard deviation =  $2.77 \text{ m s}^{-1}$ ), the classification criteria are similar. However, the positive (negative) anomaly of a U index represents a trough (ridge) anomaly event, by contrast,

the positive (negative) anomaly of a Z index represents a ridge (trough) anomaly event.

The composites of the strong trough anomaly events and strong ridge anomaly events are shown in Fig. 2. For the strong trough anomaly events, they are characterized by troughs with negative GPH anomalies at 500 hPa over the Ural Mountains (Fig. 2a), besides, cyclonic circulation anomalies at 850 hPa, with anomalous westerlies over the south of Ural Mountains (Fig. 2c). By contrast, for the strong ridge anomaly events, they are characterized by ridges with positive GPH anomalies at 500 hPa over the Ural Mountains (Fig. 2b), accompanied by anticyclonic circulation anomalies at 850 hPa, with anomalous easterlies over the south of Ural Mountains (Fig. 2d). In addition, for the strong trough anomaly events, due to the cold (warm) air advection associated with the anomalous northerly (southerly) wind over the upstream (downstream) of Ural Mountains (Fig. 2c),

there is a cold (warm) temperature anomaly over the Ural (Lake Baikal) region at 850 hPa (Fig. 2e). By contrast, for the strong ridge anomaly events, there is a warm (cold) temperature anomaly over the Ural Mountains and Barents-Kara Seas (Lake Baikal and Northeast China) region (Fig. 2f), because of the warm (cold) air advection associated with the anomalous southerly (northerly) wind over the upstream (downstream) of Ural Mountains (Fig. 2d). It indicates that the Ural circulation anomalies can directly cause anomalous climate over many regions over Eurasia.

In addition, it's notable that there are opposite anomalies between the GPH field and zonal wind field (Fig. 2). In fact, the correlation coefficients between the Z index and U index are  $-0.83$ ,  $-0.87$  and  $-0.77$  for December to February, respectively. These high negative correlation coefficients imply the quasi-geostrophic balance between the GPH field and zonal wind field over the Ural Mountains.

## 4 Theoretical model

### 4.1 Supercritical pitchfork bifurcation theory

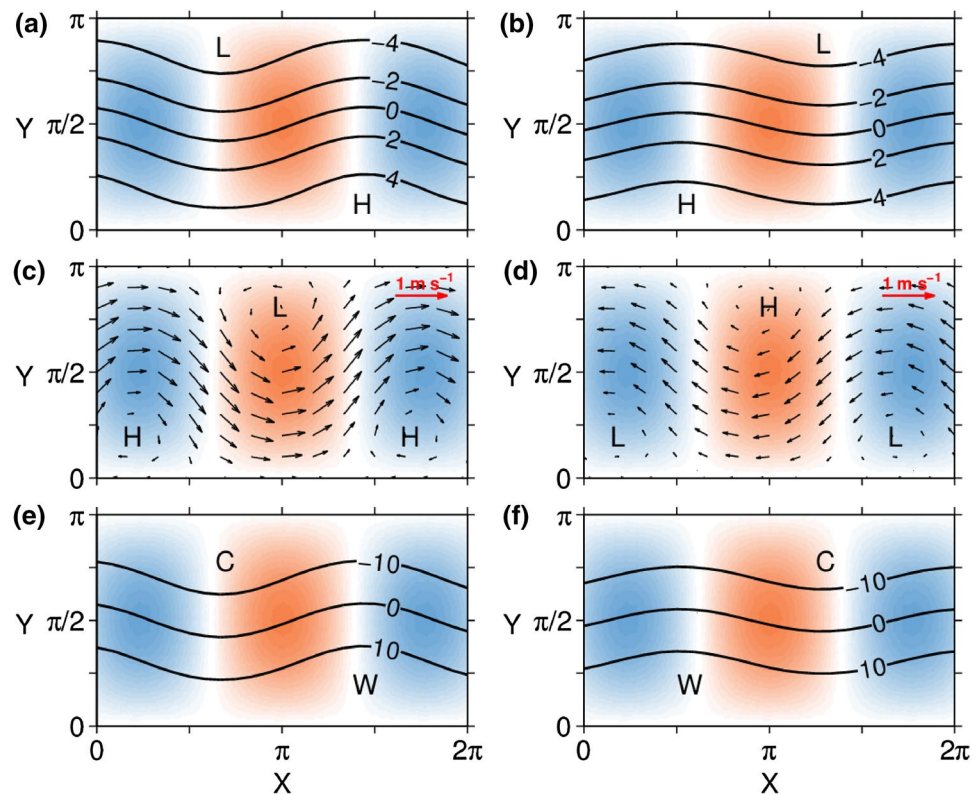
The theoretical model is based on a simple theory called “supercritical pitchfork bifurcation”. The supercritical pitchfork bifurcation is a particular type of local bifurcation, where the system transitions from one stable equilibrium to one unstable equilibrium and two stable equilibria (Steven 2000; Dijkstra 2013). A famous example is the buckling of a elastic rod (known as Euler rod; Timoshenko and Gere 1961). As shown in Fig. 4c, apply an increasing axial load to a vertical elastic rod, the relationship between the axial load,  $F$ , and the amplitude of buckling,  $x$ , is sketched in Fig. 4d (Steven 2000). The rod remains in a non-buckling state ( $x=0$ ) for a while, and this is a stable equilibrium. It finally buckles to either the left or the right ( $x<0$  or  $x>0$ ), at this point, the left-side buckling and right-side buckling are both stable equilibria, but the non-buckling is an unstable equilibrium. In other words, when the axial load is beyond the critical value, either the left-side buckling or right-side buckling can be observed, but the non-buckling cannot be observed theoretically. The rod suffers a “supercritical pitchfork bifurcation” at the critical point of buckling. The left-side buckling and right-side buckling are duplex equilibria under the same axial load. Particularly, under ideal conditions, the left-side buckling and right-side buckling are equally likely to occur, they have the same “amplitude” but opposite “phase”.

In our previous paper L18, we proposed the multiple wave phase equilibria theory. We used a low-order coupled land–atmosphere model and the model atmosphere is a two-layer quasi-geostrophic flow confined to a periodic  $\beta$  plane channel. We found that the same solar radiation and

topographic forcing may yield two types of stationary equilibrium states with opposite wave phase in the atmosphere flows: one (the other) equilibrium state has troughs (ridges) over the mountains, called trough-type (ridge-type) equilibrium. As shown in Fig. 3, the trough-type equilibrium is characterized by troughs over the west side of the mountains (positive topographic heights) at the upper layer (Fig. 3a), and the cyclonic circulation over the mountains at the lower layer (Fig. 3c), with westerlies over the south of the mountains (Fig. 3c). By contrast, the ridge-type equilibrium is characterized by ridges over the west side of the mountains at the upper layer (Fig. 3b), and the anticyclonic circulation over the mountains at the lower layer (Fig. 3d), with easterlies over the south of the mountains (Fig. 3d). In addition, the trough-type equilibrium shows a cold (warm) tongue in the atmospheric temperature field over the upstream (downstream) of the mountains (Fig. 3e), on the contrary, the ridge-type equilibrium shows a warm (cold) tongue in the atmospheric temperature field over the upstream (downstream) of the mountains (Fig. 3f).

Particularly, we pointed out that the multiple wave phase equilibria associated with trough-type and ridge-type equilibrium states originate from the orographic instability of the Hadley equilibria, which is a supercritical pitchfork bifurcation. As shown in Fig. 4a, b, the model parameter  $C_g$  represents the meridional gradient of surface net solar radiation (it can be interpreted as the difference in the surface net solar radiation between  $22.5^\circ$  and  $67.5^\circ$  N is  $2\sqrt{2} C_g$ ), this parameter controls the zonal flow in the model atmosphere (note that the parameter  $C_g$  does not represent the meridional temperature gradient,  $C_g$  indicates an external forcing). When the  $C_g$  (like the axial load,  $F$ ) is less than  $50 \text{ W m}^{-2}$ , there is only one equilibrium state called “Hadley equilibrium” (black circles). According to L18, the Hadley equilibrium is characterized by pure zonal motion without any meridional perturbations (black circles, Fig. 4a) in the upper-layer streamfunction field and horizontally motionless (black circles, Fig. 4b) in the lower-layer streamfunction field (like the non-buckling equilibrium of the elastic rod). When the  $C_g$  is greater than or equal to  $50 \text{ W m}^{-2}$ , the Hadley equilibrium is unstable (like the unstable non-buckling equilibrium of the elastic rod), there exists two new stable equilibrium states, namely, trough-type equilibrium (blue circles) and ridge-type equilibrium (red circles). The trough-type and ridge-type equilibria have the opposite wave phase, i.e., troughs (blue circles, Fig. 4a) and ridges (red circles, Fig. 4a), in the upper-layer streamfunction field, accompanied by the opposite zonal wind, i.e., westerlies (blue circles, Fig. 4b) and easterlies (red circles, Fig. 4b), in the lower-layer streamfunction field (like the left-side buckling and right-side buckling equilibria of the elastic rod). However, when the  $C_g$  is greater than  $54 \text{ W m}^{-2}$ , the

**Fig. 3** **a, b** The streamfunction fields (contours) at the upper layer, **c, d** horizontal wind fields (vectors) at the lower layer and **e, f** atmospheric temperature fields (contours) in the two-layer  $\beta$  plane channel model for the trough-type equilibrium (left panels) and ridge-type equilibrium (right panels), respectively (adapted from Li et al. 2018). The contour intervals are **a, b**  $2.0 \times 10^7 \text{ m}^2 \text{ s}^{-1}$  and **e, f** 10 K, respectively. The colored background shows the topographic height in the model, and the warm (cool) tone indicates positive (negative) regions. “H” and “L” in **a–d** represent high and low pressure, respectively. “W” and “C” in **e, f** represent warm and cold tongue, respectively



ridge-type equilibrium becomes unstable and disappears, whereas the trough-type equilibrium remains stable and still exists (supposing the material of the rod is inhomogeneous and anisotropic, under a too large axial load, the rod yields or fractures in the case of right-side buckling, whereas the rod can remain elastic buckling in the case of left-side buckling). In short, the three types of atmospheric equilibria, namely, the Hadley, trough-type and ridge-type equilibria, are analogous to the three equilibrium states that the elastic rod keeps non-buckling, left-side buckling and right-side buckling, respectively, because they both follow the supercritical pitchfork bifurcation theory.

According to L18, the Hadley equilibrium does not interact with the orography, by contrast, the trough-type and ridge-type equilibria, as the duplex equilibria, originate from the orographic instability of the Hadley equilibrium. In addition, with the increase of the parameter  $C_g$ , for the Hadley equilibrium, the model atmosphere is horizontally motionless at the lower layer (Fig. 4b), however, the zonal wind at the upper layer increases rapidly and the vertical wind shear also increases rapidly (see Figs. 11, 12 in L18, or see Supplementary Fig. S2). Moreover, when the parameter  $C_g$  reaches a critical value, the zonal wind at the upper layer and the vertical wind shear also reaches the critical values or turning points (Supplementary Fig. S2). Thus, the mechanism of the behavior of model atmospheric flow is as following:

1. When the parameter  $C_g$  is relatively small, the zonal flow at the upper layer is weak and the vertical wind shear is also small, so that the model atmosphere is baroclinic stable, the Hadley equilibrium has no flow in the lower layer, hence, the model flow does not interact with the orography, therefore, there is only one zonally symmetric equilibrium circulation (Fig. 4a, b).
2. When the parameter  $C_g$  is greater than the critical value, the zonal flow at the upper layer is strong that beyond the critical velocity, the vertical wind shear also exceeds a critical value, as a consequence, the baroclinic instability induces zonal flow in the lower layer, then the zonal flow interacts with the orography, giving rise to the orographic instability and two new equilibria: the trough-type and ridge-type equilibria (Fig. 4a, b), these duplex equilibrium circulation have opposite wave phase at the upper layer and opposite zonal wind at the lower layer (Fig. 3). The occurrence of the supercritical pitchfork bifurcation is due to the zonal flow interacting with the orography.

#### 4.2 Similarity between the theoretical model and Ural atmospheric circulation

What's more, it's notable that the characteristics of the three atmospheric equilibria in L18 are very similar to those of the three categories of Ural circulation patterns. The Hadley,

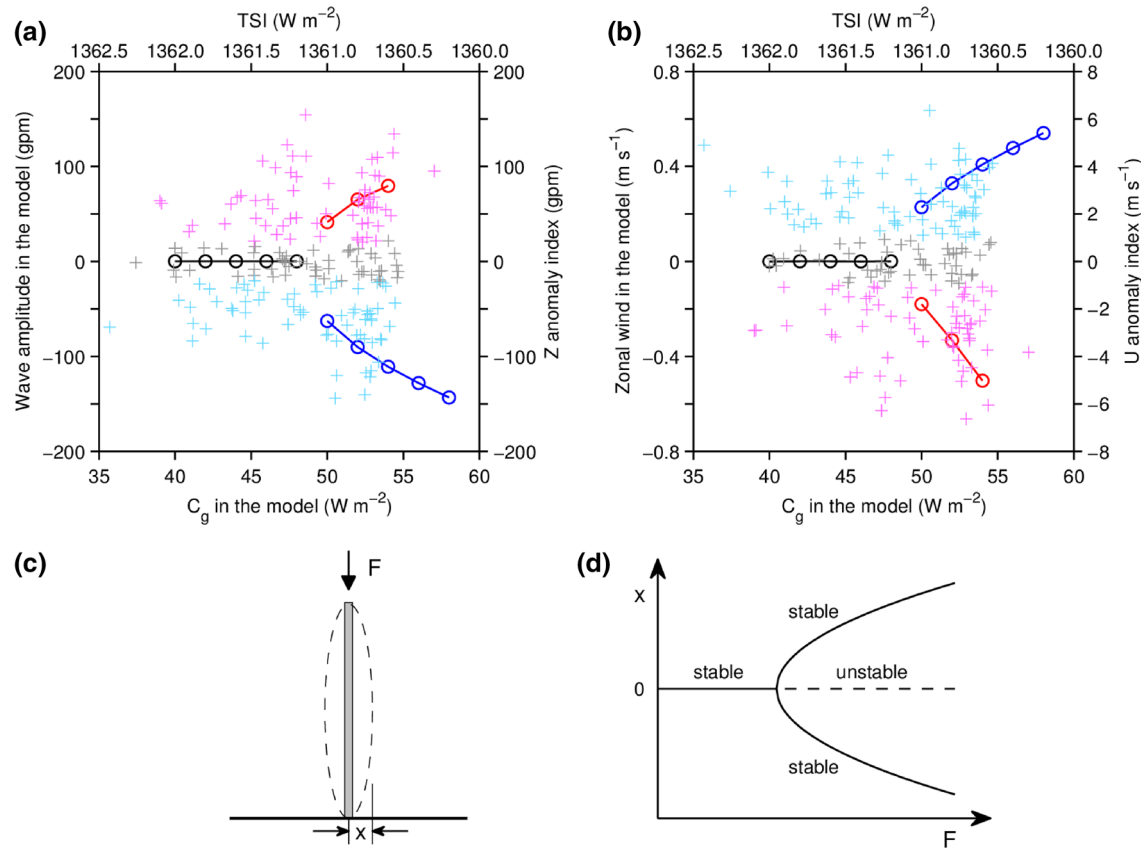


**Fig. 4** The equilibrium solutions in the model (shown by the bottom X-axis and the left Y-axis; adapted from Li et al. 2018) and the observations (shown by the top X-axis and the right Y-axis) for **a** GPH field and **b** zonal wind field. Three branches with circles show the equilibrium solutions in the model: blue, red and black circles denote the stable trough-type, ridge-type and Hadley equilibria, respectively. Pluses show the observed monthly mean atmospheric circulation patterns over the Ural Mountains: cyan, magenta and grey pluses denote the trough anomaly, ridge anomaly and neutral type events, respectively. The left Y-axis in **a** denotes the amplitude of wave components

at upper-layer GPH field in the model, the left Y-axis in **b** denotes the channel-averaged zonal wind at the lower layer in the model. Z/U anomaly index is the Z/U index that the climatological (1981–2010) mean has been removed. Note that the top X-axis in **a**, **b** is reversed. **c** A physical example for supercritical pitchfork bifurcation (Timoshenko and Gere 1961): a vertical elastic rod suffers from an increasing axial load ( $F$ ), finally the rod buckles to either the left or the right (the amplitude of buckling is  $x$ ). **d** The diagram for supercritical pitchfork bifurcation (Steven 2000): the relationship between the axial load,  $F$ , and the amplitude of buckling,  $x$

trough-type and ridge-type equilibria (Fig. 3) are very similar to the neutral type, trough anomaly and ridge anomaly of Ural circulation patterns (Fig. 2), respectively. Besides, the topographic features over the Ural region are quite similar to the model topography in L18, where the latter is an ideal sinusoidal topography with a fixed amplitude as 1.46 km (see the colored background in Fig. 3). The Urals are elongated mountains, extending from the Arctic coast to the northwestern Kazakhstan along 60° E (Fig. 1). Most mountains of the Urals rise to 500–1200 m above sea level. The West Siberian Plain and the East European Plain are located on the eastern and western side of the Ural Mountains, respectively. Therefore, the Ural region is characterized by the meridionally elongated Ural Mountains and zonally basin-mountain-basin topography. The model topography in L18 (Fig. 3) exactly resembles the real topography over the Ural region (Fig. 1).

Thus, do the behavior of Ural circulation anomalies also follow the supercritical pitchfork bifurcation theory, just like the behavior of model atmospheric flow in L18?

General circulation of the atmosphere is mainly driven by the meridional (equator-to-pole) thermal gradient at the Earth's surface. Previous studies (e.g., Soon and Legates 2013; Weng 2012; Cai and Tung 2012) suggested that the increased TSI is corresponding to the decreased temperature gradient between the Equator and the Arctic. Thus, we expect that with the decrease in TSI, the corresponding increase in meridional temperature gradient would increase the large-scale zonal flow in mid-high latitudes. Besides, the model parameter  $C_g$  and TSI both represent the solar signal which is an external forcing. Thus, to some degree, the decrease in TSI may have similar effect to the increase in the model parameter  $C_g$ . We might also show

the relationship between TSI and Ural atmospheric circulation in Fig. 4a, b. It's seen that at the same TSI value, all three types of Ural circulation patterns, namely, neutral type (grey pluses), trough anomaly (cyan pluses) and ridge anomaly (magenta pluses) can occur. It can be noticed that when TSI is about  $1361.0 \text{ W m}^{-2}$ , the observed points become sparse (especially in Fig. 4a). Similarly, the equilibrium solutions in the model also show a discontinuous zone when  $48 < C_g < 50 \text{ W m}^{-2}$ . It also can be noticed that when TSI is less than  $1360.5 \text{ W m}^{-2}$ , all of the observed three types of Ural circulation patterns suddenly disappear (there is only one magenta plus when  $\text{TSI} < 1360.5 \text{ W m}^{-2}$ ). Similarly, in the theoretical model, when  $C_g > 54 \text{ W m}^{-2}$ , the ridge-type equilibrium suddenly disappears, even though the trough-type equilibrium still exists (note that when  $\text{TSI} < 1360.5 \text{ W m}^{-2}$ , the data is lacking, thus, the observed cyan pluses do not extend to the very right side). Therefore, to some degree, there is some similarity between the theoretical model and the observations. However, the observed points are quite scattered, does the distribution of observed points really follow the supercritical pitchfork bifurcation theory?

Note that the theoretical solutions in the model (three branches with circles in Fig. 4a, b) represent equilibrium states, the trough-type and ridge-type equilibria are both stationary wave solutions. By contrast, the observed points (pluses in Fig. 4a, b) represent monthly mean atmospheric states. In the monthly mean atmospheric circulation fields, most traveling synoptic-scale waves are filtered out, and quasi-stationary planetary waves are retained. However, the monthly mean atmospheric circulation is still time-varying, it does not represent "equilibrium state". In addition, the Ural atmospheric circulation is affected by many forcing factors (e.g., Eurasian snow cover, Arctic sea ice, and Atlantic sea surface temperature), not only the solar forcing. Thus, we cannot see that all pluses are close to the three branches of equilibrium solutions in Fig. 4a, b. Nevertheless, if the supercritical pitchfork bifurcation theory really works for the mechanism of solar activity affecting Ural circulation anomalies, we should expect that the pluses have a high frequency to cluster around the three branches of equilibrium solutions.

To examine the extent to which the behavior of atmospheric circulation over the Ural Mountains agrees with the theoretical model in L18, two questions should be focused on: (1) whether the three types of Ural circulation patterns are circulation regimes or preferred circulation patterns, particularly, whether there is only one circulation regime when TSI is greater than a critical value ( $\text{TSI} > S_c$ ), whereas duplex or multiple circulation regimes when TSI is less than a critical value ( $\text{TSI} < S_c$ ); (2) when  $\text{TSI} < S_c$ , if there are duplex or multiple circulation regimes, whether the trough anomaly and ridge anomaly patterns, just like the

left-side buckling and right-side buckling of the elastic rod, are equally likely to occur at the same TSI. Statistics analyses should be used, and the two above questions are nearly equivalent to the following two questions: (1) whether the multimodality or bimodality in the PDF of the Z/U index can be detected, particularly, in the joint PDF of TSI and Z/U index, whether there is only one peak region when  $\text{TSI} > S_c$  ( $S_c$  is a critical value of TSI), whereas duplex or multiple peak regions when  $\text{TSI} < S_c$ ; (2) when  $\text{TSI} < S_c$ , if there are duplex or multiple peak regions in the joint PDF of TSI and Z/U index, whether the frequencies of occurrence for the trough anomaly and ridge anomaly events are almost equal to each other during the same TSI range. The corresponding results are presented in Sect. 5.

## 5 Statistical properties of Ural atmospheric circulation

### 5.1 The PDFs of Z and U indices

The PDFs and histograms of Z and U indices are shown in Fig. 5a, b. It's seen that the PDFs and histograms of Z and U indices both show three main peaks. These three peaks are obviously separated. For the Z index, the maximum peak occurs near 5300 gpm, the second highest peak occurs near 5350 gpm, and the third highest peak occurs near 5250 gpm (Fig. 5a). For the U index, the maximum peak occurs near  $4 \text{ m s}^{-1}$ , the second and third highest peaks occur near  $6 \text{ m s}^{-1}$  and  $1.5 \text{ m s}^{-1}$ , respectively.

However, is it possible that the multimodality in the PDF of Z/U index results from the seasonal cycle signals or long-term trends in the samples? Figure 5c, d show the PDFs and histograms of the deseasonalized and detrended Z and U indices. That is, for the 180 samples of Z/U index, firstly, the mean is removed from the individual time series (60 samples) for each month, then, the least squares trend is also removed from the individual time series for each month. Clearly, there are still three main separated peaks in the PDFs and histograms. For the Z index, the maximum peak occurs near 0 gpm, other two main peaks occur near  $-50$  and  $60 \text{ gpm}$  (Fig. 5c). For the U index, the first, second and third highest peaks occur near  $0$ ,  $2.5$  and  $-3 \text{ m s}^{-1}$ , respectively (Fig. 5d). It seems that the seasonal cycle signals and long-term trends in the samples have no remarkable effect on the PDFs and histograms of Z and U indices.

Therefore, there are robust three main PDF peaks for the Z/U index. In addition, the three PDF peaks roughly represent the neutral type, trough anomaly and ridge anomaly patterns, respectively (Fig. 5). Thus, it suggests that the three types of Ural circulation patterns are circulation regimes or preferred circulation patterns.

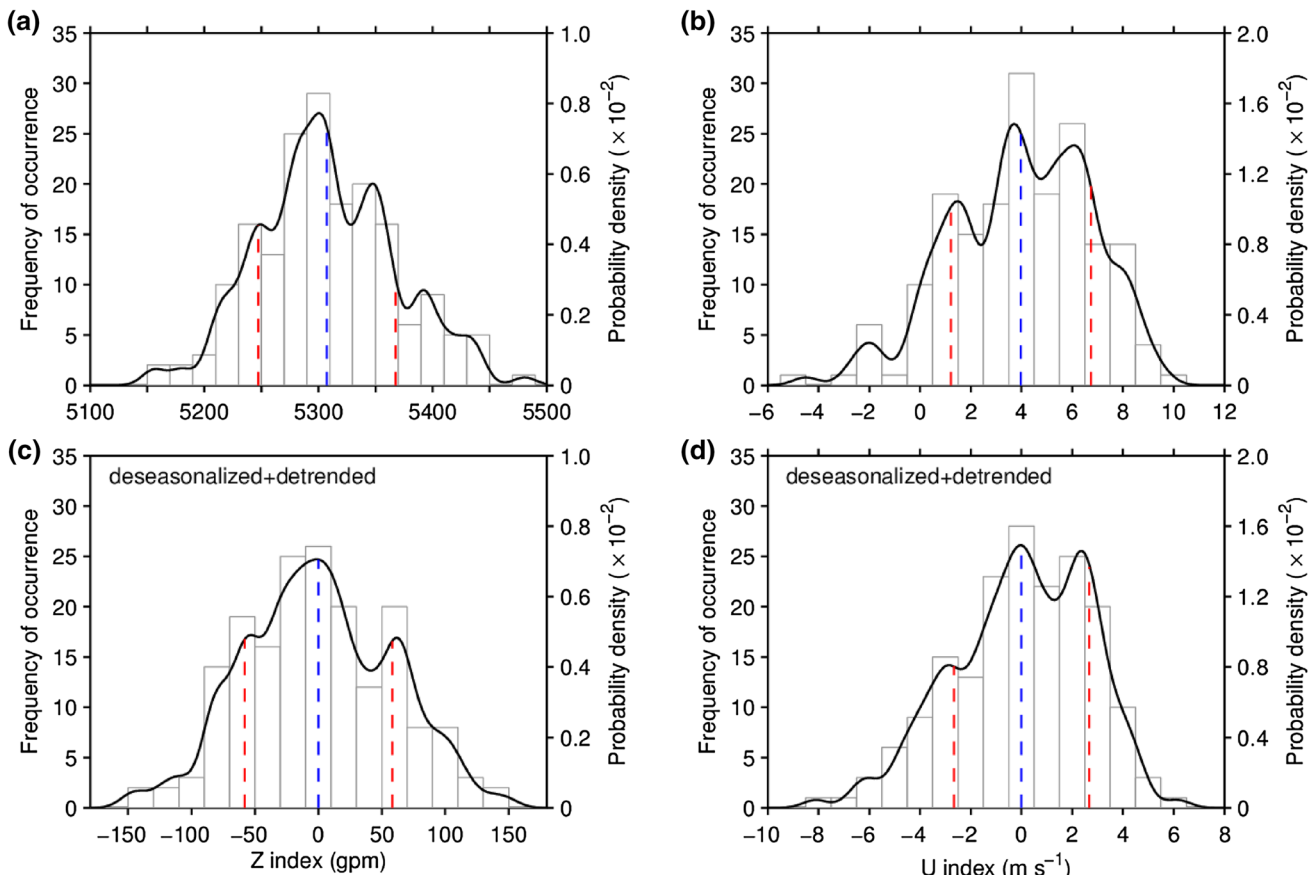


**Fig. 5** Histograms (thin bars) and PDFs (thick curves) of **a, c** Z index and **b, d** U index. **a, b** Original; **c, d** deseasonalized and detrended Z and U indices, respectively. The Z (U) index is partitioned with a bin width of 20 gpm (1.0  $m s^{-1}$ ) for the histogram estimates and 1.0 gpm (0.1  $m s^{-1}$ ) for the probability density estimates. The bandwidth of

the smoothing window for the probability density estimate of Z (U) index is 10 gpm (0.5  $m s^{-1}$ ). Vertical dashed lines show the statistics properties of the Z index (left panels) and the U index (right panels): blue lines show the mean, red lines show one standard deviation below and above the mean, respectively

The joint (bidimensional) PDF of TSI and the Z index is shown in Fig. 6a. It's seen that at the same TSI, the three circulation patterns can coexist. There are several peak regions of the joint PDF. When  $TSI > 1360.9 W m^{-2}$ , there is only one peak region which is long and narrow, this peak region is near the mean value of the Z index, thus, this peak region represents the neutral type pattern. As the TSI decreases, when  $TSI < 1360.9 W m^{-2}$ , there are three distinguishable peak regions, the middle one represents the neutral type pattern, the lower one and the upper one are both near the standard deviation lines, thus, they represent the trough anomaly and ridge anomaly patterns, respectively. Apparently, the joint PDF of TSI and the Z index shows a three-tine-pitchfork-like or trident-like pattern that exactly resembles the supercritical pitchfork bifurcation diagrams in Fig. 4. As for the joint PDF of TSI and the U index (Fig. 6b), when  $TSI > 1360.9 W m^{-2}$ , there is also only one peak region that represents the neutral type pattern. However, when  $TSI < 1360.9 W m^{-2}$ , there are only two separated peak regions, the lower peak region represents the ridge anomaly

pattern, the upper peak region is quite large and represents both the neutral type and trough anomaly patterns. The JRA-55 reanalysis shows similar results, but for the joint PDF of TSI and Z/U indices, they both show three distinguishable peak regions when  $TSI < 1360.9 W m^{-2}$  (see Supplementary Fig. S1). In addition, when the Z and U indices are deseasonalized and detrended, the joint PDFs of TSI and Z/U indices both show a clear three-tine-pitchfork-like or trident-like pattern (Fig. 6c, d).

Therefore, during relatively high TSI ( $1360.9 < TSI < 1361.4 W m^{-2}$ ), the neutral type pattern is the single circulation regime, due to the only one joint PDF peak region (Fig. 6). By contrast, during relatively low TSI ( $TSI < 1360.9 W m^{-2}$ ), the neutral type, trough anomaly and ridge anomaly patterns are all circulation regimes, due to the multiple joint PDF peak regions (Fig. 6). These results are roughly consistent with the theoretical model (Fig. 4), which shows single equilibrium at relatively small  $C_g$  values ( $C_g < 50 W m^{-2}$ ), whereas multiple equilibria at relatively large  $C_g$  values

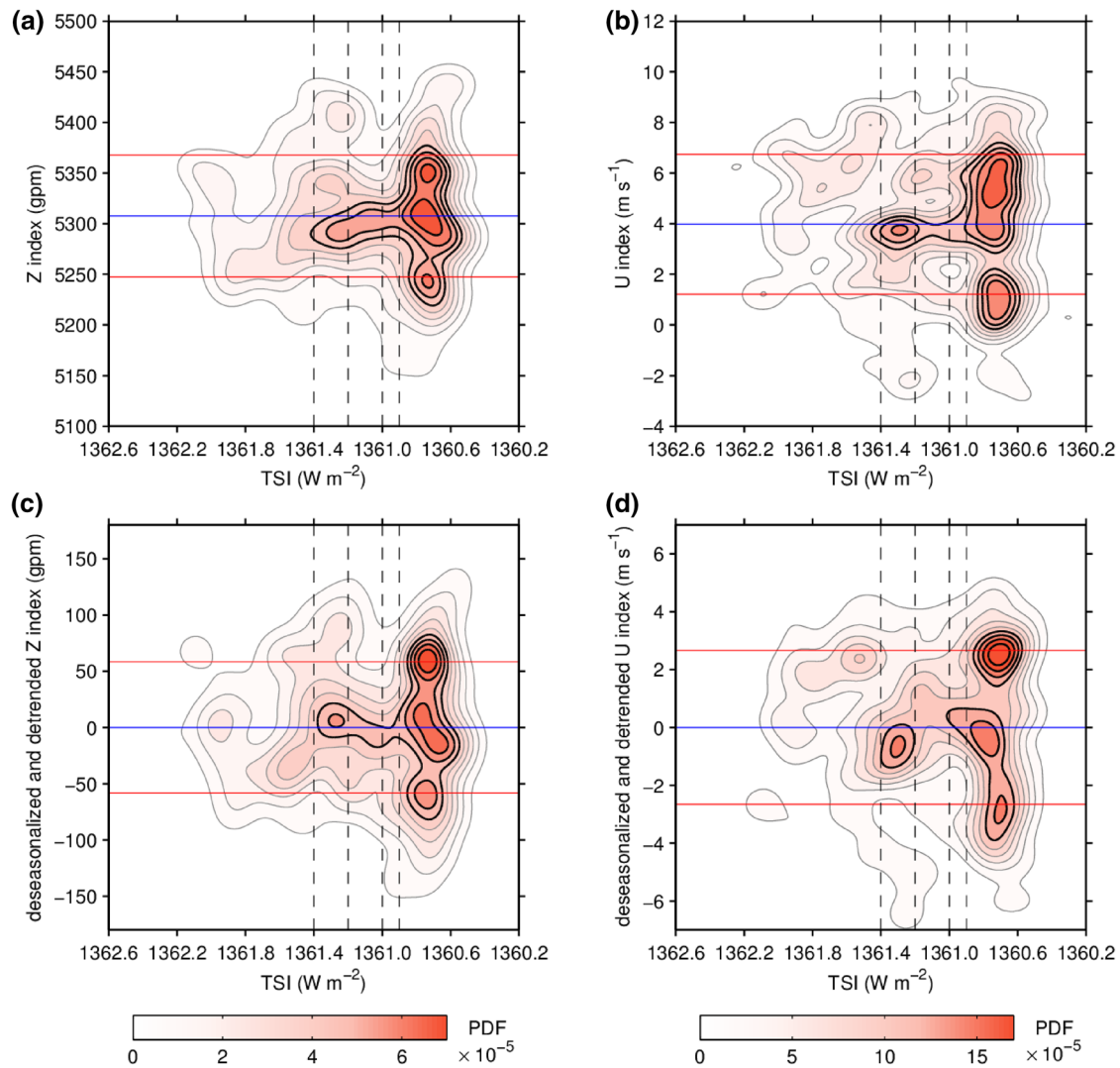


**Fig. 6** The joint PDFs of **a** Z index and TSI; **b** U index and TSI; **c** deseasonalized and detrended Z index and TSI; **d** deseasonalized and detrended U index and TSI. The Z index, U index and TSI are partitioned with a bin width of 1.0 gpm, 0.1  $\text{m s}^{-1}$  and 0.01  $\text{W m}^{-2}$  for the joint probability density estimates, with the bandwidths of smoothing window of 15 gpm, 0.5  $\text{m s}^{-1}$ , 0.1  $\text{W m}^{-2}$ , respectively. Horizontal solid lines show the statistics properties of the Z index (left panels)

and the U index (right panels): blue lines show the mean, red lines show one standard deviation below and above the mean, respectively. Four vertical black dashed lines indicate that TSI is equal to 1360.9, 1361.0, 1361.2 and 1361.4  $\text{W m}^{-2}$ , respectively. To highlight the peak regions, thick black isolines indicate the 60%, 70%, 80% and 90% of the maximum value of the joint PDF. Note that the X-axis is reversed

( $50 \leq C_g \leq 54 \text{ W m}^{-2}$ ).  $\text{TSI} = 1360.9 \text{ W m}^{-2}$  can be a critical value, just like the critical value  $C_g = 50 \text{ W m}^{-2}$  in the theoretical model.

However, strictly speaking, when TSI is below the critical value  $1360.9 \text{ W m}^{-2}$ , the joint PDF peak region that represents the neutral type pattern shown in Fig. 6 should not occur. Because in the theoretical model, when the parameter  $C_g$  is beyond the critical value  $50 \text{ W m}^{-2}$ , the Hadley equilibrium becomes unstable (Fig. 4a, b). This problem will be addressed in Sect. 6.1.

## 5.2 The frequency of occurrence for Ural circulation patterns

Next, we examine the frequency of occurrence for the Ural circulation patterns with respect to TSI. Because  $1360.9 \text{ W m}^{-2}$  can be a critical value of TSI, we will examine that when  $\text{TSI} < 1360.9 \text{ W m}^{-2}$ , whether the frequencies of occurrence for the trough anomaly and ridge anomaly events are almost equal to each other during the same TSI range.

**Table 1** Cumulative frequency of Ural circulation patterns when  $\text{TSI} \leq S$ 

$S (\text{W m}^{-2})$	Based on the Z index					Based on the U index				
	TA		NT	RA		TA		NT	RA	
	Strong	All		All	Strong	Strong	All		All	Strong
1360.2	0	<b>0</b>	0	<b>0</b>	0	0	<b>0</b>	0	<b>0</b>	0
1360.3	0	<b>0</b>	0	<b>1</b>	1	0	<b>0</b>	0	<b>1</b>	1
1360.4	0	<b>0</b>	0	<b>1</b>	1	0	<b>0</b>	0	<b>1</b>	1
1360.5	0	<b>0</b>	0	<b>1</b>	1	0	<b>0</b>	0	<b>1</b>	1
1360.6	1	<b>5</b>	1	<b>5</b>	3	2	<b>5</b>	1	<b>5</b>	3
1360.7	4	<b>14</b>	4	<b>14</b>	6	4	<b>14</b>	4	<b>14</b>	9
1360.8	15	<b>29</b>	10	<b>28</b>	12	11	<b>30</b>	8	<b>29</b>	15
1360.9	16	<b>33</b>	13	<b>32</b>	12	11	<b>34</b>	12	<b>32</b>	17
1361.0	20	40	16	33	13	13	39	15	35	18
1361.1	20	43	21	36	13	15	43	17	40	19
1361.2	21	46	22	39	15	15	47	18	42	21
1361.3	22	52	25	49	20	17	52	23	51	25
1361.4	22	54	26	53	22	17	52	25	56	25
1361.5	23	58	29	59	24	22	58	28	60	27
1361.6	24	64	30	61	26	23	63	29	63	28
1361.7	25	66	31	63	26	24	66	29	65	28
1361.8	25	69	31	63	26	24	69	29	65	28
1361.9	27	72	32	64	26	25	73	29	66	28
1362.0	28	75	33	66	26	26	75	30	69	28
1362.1	28	76	33	69	26	27	76	31	71	30
1362.2	28	76	33	69	26	27	76	31	71	30
1362.3	28	76	34	69	26	27	77	31	71	30
1362.4	28	76	34	69	26	27	77	31	71	30
1362.5	29	77	34	69	26	28	78	31	71	30

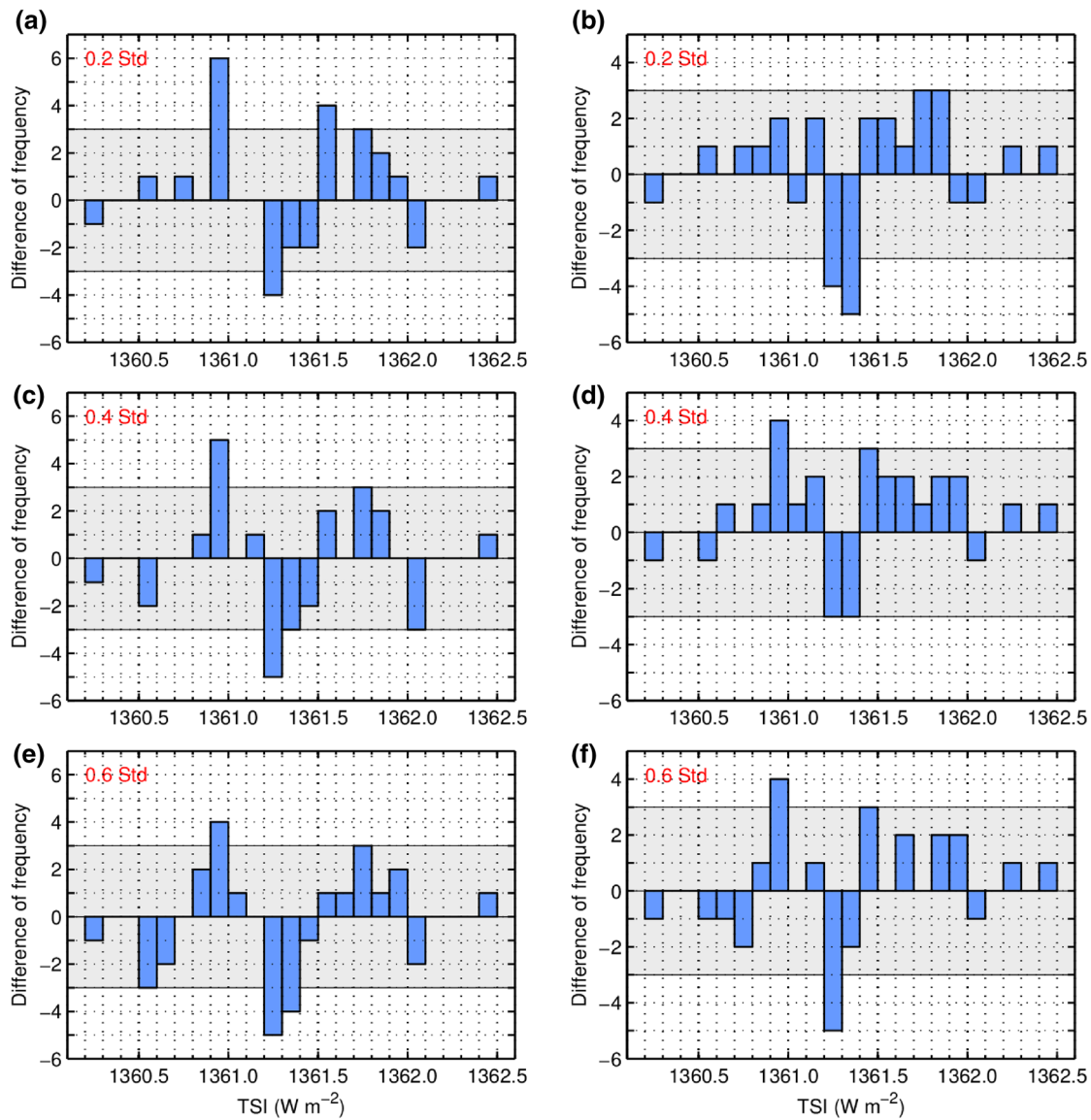
“TA”, “NT” and “RA” denotes trough anomaly, neutral type and ridge anomaly, respectively. The NCEP–NCAR reanalysis is used here

Table 1 shows the cumulative frequency of Ural circulation patterns when TSI is less than or equal to a certain value ( $\text{TSI} \leq S$ ). The TSI varies from 1360.2 to 1362.5  $\text{W m}^{-2}$ , so “when  $\text{TSI} \leq S$ ” means “when  $1360.2 \leq \text{TSI} \leq S$ ”. For an arbitrary value of  $S$  which lies in the interval  $1360.2 < S \leq 1360.9 \text{ W m}^{-2}$ , when  $1360.2 \leq \text{TSI} \leq S \text{ W m}^{-2}$ , the cumulative frequencies of trough anomaly and ridge anomaly events are almost equal to each other (see bold numbers in Table 1). For example, when  $S = 1360.9 \text{ W m}^{-2}$  (i.e.,  $1360.2 \leq \text{TSI} \leq 1360.9 \text{ W m}^{-2}$ ), the ratio of the cumulative frequency of trough/ridge anomaly events is 33:32 (34:32) based on the Z (U) index. When  $1360.2 \leq S \leq 1360.9 \text{ W m}^{-2}$ , the differences between the cumulative frequencies of trough anomaly and ridge anomaly events when  $\text{TSI} \leq S$  are always no more than 1 based on the Z index, and 2 based on the U index. This is because for each minimum interval of  $0.1 \text{ W m}^{-2}$  of TSI, trough anomaly and ridge anomaly events also almost have the same frequencies. For example, when  $1360.6 < \text{TSI} \leq 1360.7 \text{ W m}^{-2}$ , the frequencies of trough anomaly and ridge anomaly events are both 9 (i.e., 14 minus 5), no matter based on the Z index or U index. The

JRA-55 reanalysis shows consistent results (see Supplementary Table S1). Therefore, when TSI is less than the critical value  $1360.9 \text{ W m}^{-2}$ , the trough anomaly and ridge anomaly events almost have the same cumulative frequencies during the same TSI range.

In addition, during each interval of  $0.1 \text{ W m}^{-2}$  of TSI, the differences between the cumulative frequencies of trough anomaly and ridge anomaly events based on the Z and U indices are shown in Fig. 7a, b. Clearly, when  $\text{TSI} < 1360.9 \text{ W m}^{-2}$ , the differences between the cumulative frequencies of trough anomaly and ridge anomaly events are always no more than 1, no matter based on the Z index or U index.

Note that the classification criterion for the neutral type and anomaly events in Table 1, Fig. 7a, b is based on the 0.2 standard deviation of the Z/U index. If the 0.4 standard deviation of the Z/U index is used as the classification criterion, when  $\text{TSI} < 1360.9 \text{ W m}^{-2}$ , the differences between the cumulative frequencies of trough anomaly and ridge anomaly events are always no more than 2 (Fig. 7c, d). If the 0.6 standard deviation of the Z/U index is used as the



**Fig. 7** The differences between the cumulative frequencies of trough anomaly and ridge anomaly events (the former minus the latter) during each interval of  $0.1 \text{ W m}^{-2}$  of TSI based on the Z index (left panels) and the U index (right panels), respectively. The classification

criterion for a trough/ridge anomaly event is based on **a, b** 0.2 standard deviation, **c, d** 0.4 standard deviation, **e, f** 0.6 standard deviation of the Z or U index. Gray shaded areas indicate the differences between the cumulative frequencies are less than or equal to 3

classification criterion, the corresponding differences are always no more than 3 (Fig. 7e, f).

Moreover, Fig. 7 also shows that no matter what classification criterion is used, during two intervals of TSI, namely,  $1360.9\text{--}1361.0 \text{ W m}^{-2}$  and  $1361.2\text{--}1361.4 \text{ W m}^{-2}$ , the differences between the cumulative frequencies of trough anomaly and ridge anomaly events are almost always more than 3. During the TSI range  $1361.2\text{--}1361.4 \text{ W m}^{-2}$ , the differences between the cumulative frequencies of trough anomaly and ridge anomaly events are always negative, it indicates the ridge anomaly events have more frequencies to occur than the trough anomaly events. Meanwhile, the joint PDF of TSI

and Z/U index just shows a peak region during the TSI range  $1361.2\text{--}1361.4 \text{ W m}^{-2}$  (Fig. 6b-d), thus, this TSI range may be special. During the TSI range  $1360.9\text{--}1361.0 \text{ W m}^{-2}$ , the differences between the cumulative frequencies of trough anomaly and ridge anomaly events are always positive, it indicates the trough anomaly events have more frequencies to occur than the ridge anomaly events. Meanwhile,  $1360.9 \text{ W m}^{-2}$  is exactly the critical value of TSI we found in Sect. 5.1. Thus, the TSI interval  $1360.9\text{--}1361.0 \text{ W m}^{-2}$  is important, it is just like the discontinuous interval of  $C_g$  ( $48 < C_g < 50 \text{ W m}^{-2}$ , Fig. 4). In crossing the discontinuous interval of  $C_g$  from low values to high values, the model

atmosphere transitions from one equilibrium state to multiple equilibrium states (Fig. 4). Similarly, in crossing the discontinuous interval of TSI ( $1360.9\text{--}1361.0\text{ W m}^{-2}$ ) from high values to low values, the observed Ural atmospheric circulation transitions from one circulation regime to multiple circulation regimes (Fig. 6).

To sum up, statistics analyses above show that: (1) three main peaks in the PDF of the Z/U index can be detected (Fig. 5), particularly,  $S_c = 1360.9\text{ W m}^{-2}$  is a critical value of TSI, in the joint PDF of TSI and the Z/U index, there is only one peak region when  $\text{TSI} > S_c$ , whereas multiple peak regions when  $\text{TSI} < S_c$  (Fig. 6); (2) when  $\text{TSI} < S_c$ , the frequencies of occurrence for the trough anomaly and ridge anomaly events are almost equal to each other during the same TSI range (Table 1, Fig. 7). Therefore, to some degree, the behavior of circulation anomalies over the Ural Mountains follows the supercritical pitchfork bifurcation theory, the trough anomaly and ridge anomaly patterns under the solar forcing, just like the left-side buckling and right-side buckling of the elastic rod under an axial load, should be equally likely to occur. When the TSI is less than the critical value  $1360.9\text{ W m}^{-2}$ , the trough anomaly and ridge anomaly patterns over the Ural Mountains can be considered duplex equilibria at the same TSI.

## 6 The physical mechanism

In the theoretical model, the occurrence of the supercritical pitchfork bifurcation is due to the zonal flow interacting with the orography. We expect that the physical mechanism of solar activity inducing the atmospheric circulation anomalies over the Ural Mountains is similar to that in the theoretical model. Thus, to explore the physical mechanism of solar activity inducing Ural circulation anomalies, three questions should be focused on: (1) Does the interaction between the large-scale zonal flow and the Ural Mountains really work for the mechanism of Ural circulation anomalies? (2) Where is the key region for the flow-mountains interaction? (3) How does the solar activity affect the large-scale zonal flow over the Ural region, hence inducing the Ural circulation anomalies? The corresponding results are presented as follows.

### 6.1 The orographic effect of Ural Mountains

If the interaction between the large-scale zonal flow and the Ural Mountains really works for the mechanism of Ural circulation anomalies, we should get these results: (1) Without the orographic effect of Ural Mountains, the pitchfork-like pattern in the joint PDF of TSI and the Z/U index shown in Fig. 6 should not occur; (2) With the orographic effect of Ural Mountains, to strictly follow the supercritical pitchfork

bifurcation theory, the joint PDF of TSI and the Z/U index should show a two-tine-pitchfork-like pattern. That is, when TSI is below the critical value  $1360.9\text{ W m}^{-2}$ , the joint PDF peak region that represents the neutral type pattern shown in Fig. 6 should not occur.

Note that, for all the results above, the U index is defined as the area-averaged zonal wind at 850 hPa over the domain ( $45^\circ\text{--}55^\circ\text{ N}, 40^\circ\text{--}80^\circ\text{ E}$ , Fig. 2c, d), this region is quite large and it is on the south of Ural Mountains. Thus, the zonal flow over some parts of this region is not necessarily affected by the orographic effect of Ural Mountains.

We have chosen another nine regions around the Ural Mountains, their locations are shown in Figs. 1 and 2c, d. The region A ( $65^\circ\text{--}75^\circ\text{ N}, 30^\circ\text{--}45^\circ\text{ E}$ ), region B ( $65^\circ\text{--}75^\circ\text{ N}, 45^\circ\text{--}60^\circ\text{ E}$ ), region C ( $65^\circ\text{--}75^\circ\text{ N}, 60^\circ\text{--}75^\circ\text{ E}$ ) and region D ( $65^\circ\text{--}75^\circ\text{ N}, 75^\circ\text{--}90^\circ\text{ E}$ ) are located in the same latitudes. The region A and B are to/on the northwest of Ural Mountains, the regions C and D are on/to the northeast of Ural Mountains. Figure 2c, d show the composite zonal wind anomalies at 850 hPa cover these four regions. The joint PDFs of TSI and the zonal wind over the regions A and D both do not show a pitchfork-like pattern (Fig. 8a, d). By contrast, the corresponding joint PDF for the region B apparently shows a three-tine-pitchfork-like pattern (Fig. 8b): when TSI is above  $1360.9\text{--}1361.0\text{ W m}^{-2}$  (the discontinuous interval of TSI), there are two separated peak regions that both represent the neutral type pattern, besides, when TSI is below  $1360.9\text{--}1361.0\text{ W m}^{-2}$ , there are three distinguishable peak regions that represent the neutral type, trough anomaly and ridge anomaly patterns, respectively. In Fig. 8c, the joint PDF of TSI and the zonal wind over the region C apparently shows a two-tine-pitchfork-like pattern: when TSI is above  $1360.9\text{--}1361.0\text{ W m}^{-2}$ , there is only one peak region that represents the neutral type pattern, besides, when TSI is below  $1360.9\text{--}1361.0\text{ W m}^{-2}$ , there are only two peak regions that represent the trough anomaly and ridge anomaly patterns, respectively. Noteworthily, when TSI is below the critical value  $1360.9\text{ W m}^{-2}$ , the joint PDF peak region that represents the neutral type pattern shown in Fig. 6 does not occur in Fig. 8c now.

The region E ( $50^\circ\text{--}60^\circ\text{ N}, 40^\circ\text{--}50^\circ\text{ E}$ ), region F ( $50^\circ\text{--}60^\circ\text{ N}, 50^\circ\text{--}60^\circ\text{ E}$ ), region G ( $50^\circ\text{--}60^\circ\text{ N}, 60^\circ\text{--}70^\circ\text{ E}$ ) and region H ( $50^\circ\text{--}60^\circ\text{ N}, 70^\circ\text{--}80^\circ\text{ E}$ ) are also located in the same latitudes (Fig. 1). The regions E and F are to/on the west of Ural Mountains, the regions G and H are on/to the east of Ural Mountains. Figure 2c, d show the composite zonal wind anomalies at 850 hPa also cover these four regions. However, the joint PDF of TSI and the zonal wind over the region E obviously does not show a pitchfork-like pattern (Fig. 8e), whereas the corresponding joint PDFs for the regions F and G both show a two-tine-pitchfork-like pattern (Fig. 8f, g), which are similar to that in Fig. 8c. But in Fig. 8h, the two-tine-pitchfork-like pattern is apparently

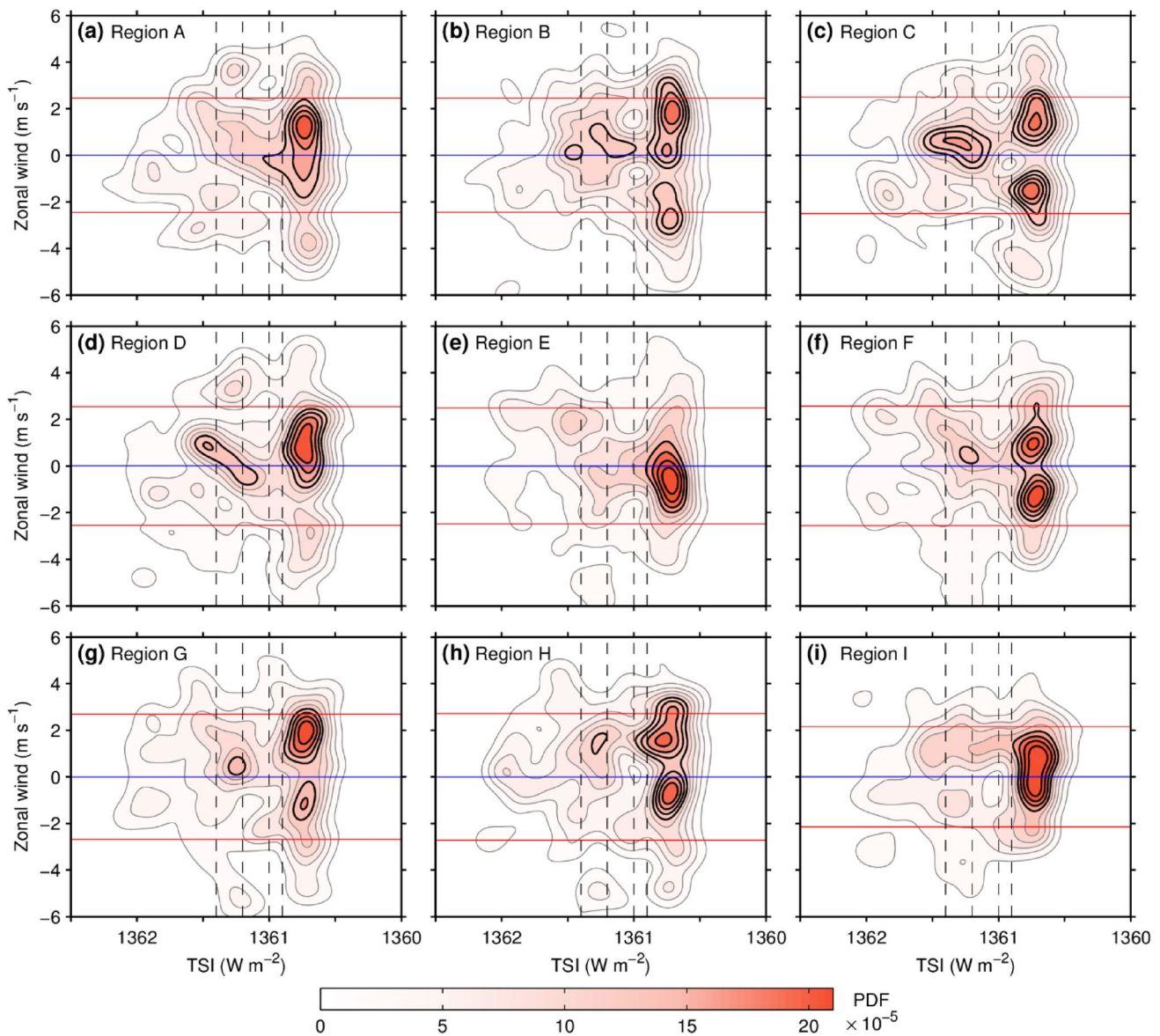


**Fig. 8** As in Fig. 6d, but for the joint PDFs of TSI and the area-averaged zonal wind at 850 hPa that defined over the **a** Region A, **b** Region B, **c** Region C, **d** Region D, **e** Region E, **f** Region F, **g** Region

**g, h** Region H and **i** Region I. The locations of the nine regions are shown in Figs. 1 and 2c, d. All of the zonal wind are deseasonalized and detrended

distorted. That is, when TSI is above  $1360.9\text{--}1361.0 \text{ W m}^{-2}$ , the only one PDF peak region is far away from the mean value line (blue line), thus, this one PDF peak region represents the trough anomaly pattern instead of the neutral type pattern.

The regions A, B, C and D are located in the same latitudes, the regions E, F, G and H are also located in the same latitudes (Fig. 1). However, the joint PDF of TSI and the zonal wind over the regions B, C, F and G obviously show a three-tine-pitchfork-like or two-tine-pitchfork-like pattern, by contrast, the regions A, D, E and H do not (Fig. 8). The different results for these eight regions can be explained

as follows: Compared with the regions A, D, E and H, the regions B, C, F and G are more close to the Ural Mountains (Fig. 1), the interaction between the large-scale zonal flow and Ural Mountains should have sufficiently high impact on the atmospheric circulation over the regions B, C, F and G. On the contrary, the regions A, D, E and H are far away from the Ural Mountains, the orographic effect of Ural Mountains on the atmospheric circulation over these four regions should be weak.

In addition, although the region I ( $57.5^{\circ}\text{--}67.5^{\circ} \text{ N}$ ,  $50^{\circ}\text{--}70^{\circ} \text{ E}$ ) is on the north of Ural Mountains (Fig. 1), Fig. 2c, d show the composite zonal wind anomalies at

850 hPa are very weak over the region I (the magenta box), because the region I is exactly in the central of the anomalous cyclonic and anticyclonic circulation. Thus, the interaction between the large-scale zonal flow and Ural Mountains should have weak effect on the atmospheric circulation over the region I. As a result, the corresponding joint PDF for the region I also does not show a pitchfork-like pattern (Fig. 8i).

Therefore, the interaction between the large-scale zonal flow and the Ural Mountains indeed works for the mechanism of Ural circulation anomalies, particularly, the joint PDF of TSI and the zonal wind over some regions (e.g. the regions C, F and G) show a two-tine-pitchfork-like pattern, generally agreeing with the supercritical pitchfork bifurcation theory.

## 6.2 The key region for the flow-mountains interaction

The interaction between the large-scale zonal flow and the Ural Mountains should occur over a key region, and the large-scale zonal flow over this key region should be noticeably affected by the solar activity. To find this key region, we should investigate the effect of solar activity on the large-scale zonal flow over the Ural region. We can compare the differences between the atmospheric circulation during high TSI months and that during low TSI months (high minus low), as shown in Figs. 9 and 10. High (low) TSI months are selected when  $TSI \geq 1361.9$  ( $\leq 1360.6$ )  $W m^{-2}$ , with a sample size of 12 (11).

Compared with low TSI months, during high TSI months, there are three main negative GPH anomaly centers in mid-high latitudes at 500 hPa (Fig. 9a), they are located over the Northern-Eastern Europe, the North Pacific and the North Atlantic, respectively. They indicate stronger-than-normal troughs over the Europe, the North Pacific and the North Atlantic. Similarly, there are also three main negative sea level pressure anomaly centers in mid-high latitudes (Fig. 9c). Focus on the Ural region, it is seen the stronger-than-normal European trough is corresponding to the negative sea level pressure anomaly over the Ural region (Fig. 9c), it indicates the northeastern Icelandic low is stronger than normal and the northwestern Siberian High is weaker than normal. Meanwhile, this negative sea level pressure anomaly center should result in the change in the horizontal pressure gradient, hence, it leads to stronger-than-normal westerlies over a belt area from Britain to the Caspian Sea (warm tone shading in Fig. 9d, f) and weaker-than-normal westerlies over the northern region of Ural Mountains (cool tone shading in Fig. 9d, f). Note that the weaker-than-normal westerlies just cover the region A and region B (see two blue boxes in Fig. 9d). In addition, during high TSI months, the zonal wind near the equatorward (poleward) flank of the subtropical westerly jet is stronger

(weaker) than normal (Figs. 9b, 10f), indicating a equatorward shift of the subtropical westerly jet. However, the zonal wind at 250 hPa near the Ural region has little change (Fig. 9b), the weaker-than-normal westerlies near the Ural Mountains only occur in the lower and middle troposphere: below 400 hPa along the 70° N (ca. 60° E, Fig. 10b), below 850 hPa along the 60° N (ca. 60° E, Fig. 10d), and below 300 hPa along the 45° E (ca. 60° N, Fig. 10f). Therefore, the large-scale zonal flow in the lower-middle troposphere over the northern region of Ural Mountains (e.g., the regions A and B) is noticeably affect by the solar activity.

Although the solar activity can affect the zonal wind over the regions A and B, the joint PDF of TSI and the zonal wind over the region B shows a pitchfork-like pattern (Fig. 8b), but that for the region A does not (Fig. 8a), because the region A is far away from the Ural Mountains, whereas the region B is close to the Ural Mountains (Fig. 1). Thus, the region B may be a key region for the interaction between the large-scale zonal flow and the Ural Mountains.

We expect that the mechanism of the flow-mountains interaction over the region B under the impact of solar activity should be somewhat similar to that in the theoretical model. In the theoretical model, for the Hadley equilibrium, with the increase of the parameter  $C_g$ , the zonal wind at the upper layer and the vertical wind shear both increase rapidly until they reach the critical velocities, then the Hadley equilibrium becomes unstable and the zonal flow interacting with the orography produces two new equilibria (Supplementary Fig. S2). Figure 11 shows the joint PDFs of TSI and the zonal wind at different pressure level over the region B. It's seen that for the zonal wind at 925 hPa and 850 hPa (Fig. 11b, c), when TSI is above  $1360.9$ – $1361.0 W m^{-2}$ , the joint PDFs both show one large peak region near the blue line, this peak region represents the “neutral type pattern”. It is noticeable that this peak region obviously tilts to the right, indicating the decrease in TSI is roughly corresponding to the increase in the zonal wind. Besides, this peak region does not cross the discontinuous interval of TSI ( $1360.9$ – $1361.0 W m^{-2}$ ) to the right, indicating there exists the critical velocity for the increasing zonal wind. However, for the zonal wind at 1000 hPa and 700 hPa (Fig. 11a, d), when TSI is above  $1360.9$ – $1361.0 W m^{-2}$ , the joint PDFs do not show similar tilted peak region. In addition, when TSI is below  $1360.9$ – $1361.0 W m^{-2}$ , the joint PDF of TSI and the zonal wind at 925 hPa shows two separable peak regions which just represent the “trough anomaly” and “ridge anomaly” patterns (Fig. 11b), suggesting the “neutral type pattern” becomes unstable and the large-scale zonal flow interacting with the Ural Mountains produces two new circulation patterns. By contrast, when TSI is below  $1360.9$ – $1361.0 W m^{-2}$ , the joint PDF of TSI and the zonal wind at 850 hPa shows three separable peak regions

**Fig. 9** The differences between the composites of **a** GPH anomaly at 500 hPa, **c** sea level pressure anomaly, **e** air temperature anomaly at 1000 hPa, and zonal wind anomaly **b** at 250 hPa, **d** at 850 hPa, **f** at 1000 hPa that during high TSI months and those during low TSI months (high minus low), respectively. The black contour lines show the mean of 180 samples (i.e., the climatological mean) for **a** GPH, **c** sea level pressure, **e** 0 °C contour, **b** 30 m s<sup>-1</sup> contours and **d**, **f** 0 m s<sup>-1</sup> contours at corresponding level, respectively. The contour intervals and ranges are **a** 100 gpm and 5100–5700 gpm, **c** 5 hPa and 1000–1030 hPa, respectively. The thick black lines in **c** indicates 1020 hPa contours, and contours that less than 1020 hPa are dashed. Red boxes enclose the region of Ural Mountains, and zoomed in for **d**, **f**. The dotted areas indicate the differences exceed the 95% confident level

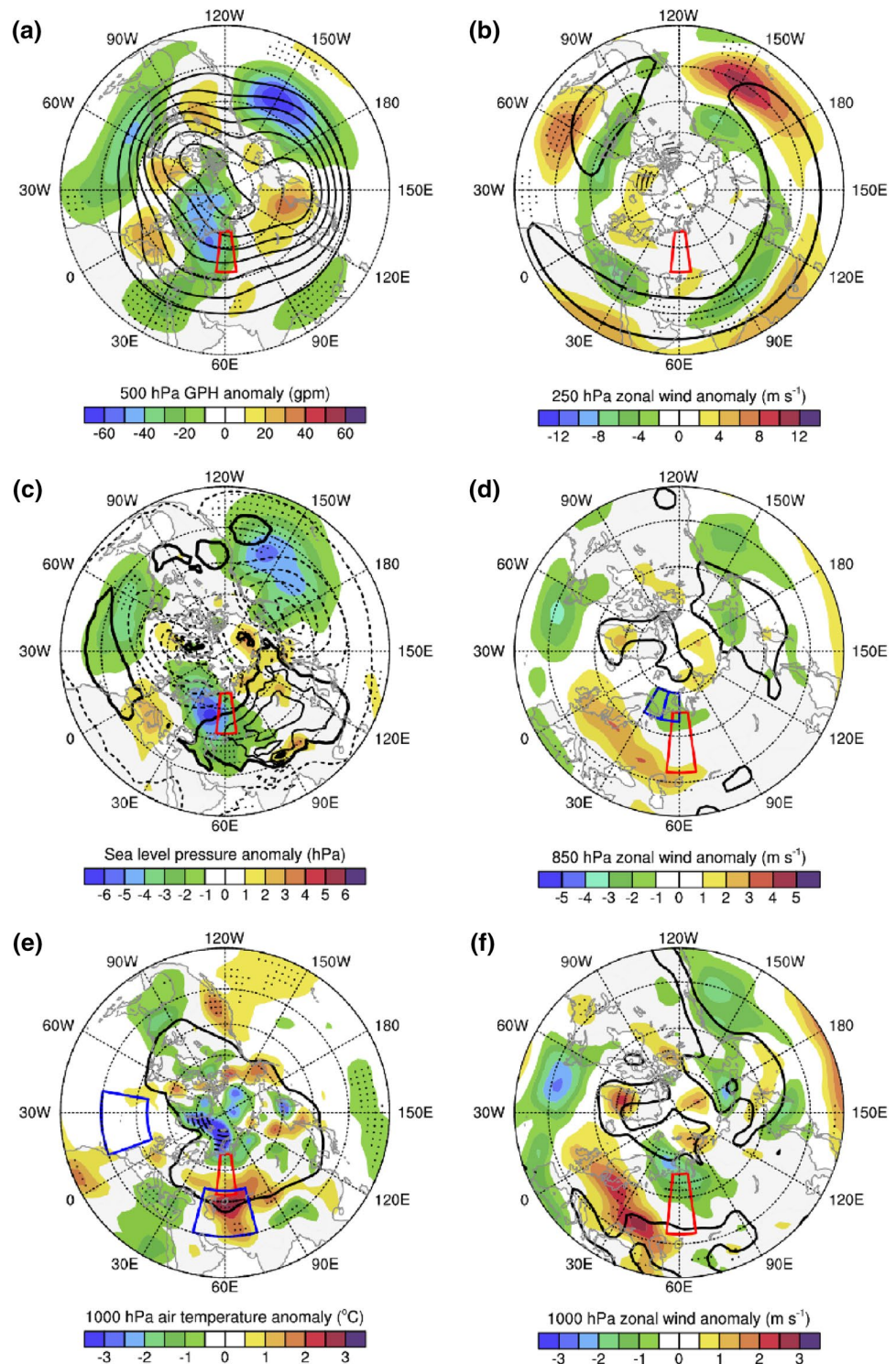


(Fig. 11c). Thus, the zonal wind at 925 hPa over the region B can be an indicator of the flow-mountains interaction under the impact of solar activity.

Therefore, the solar activity can affect the large-scale zonal flow in the lower-middle troposphere over the northern

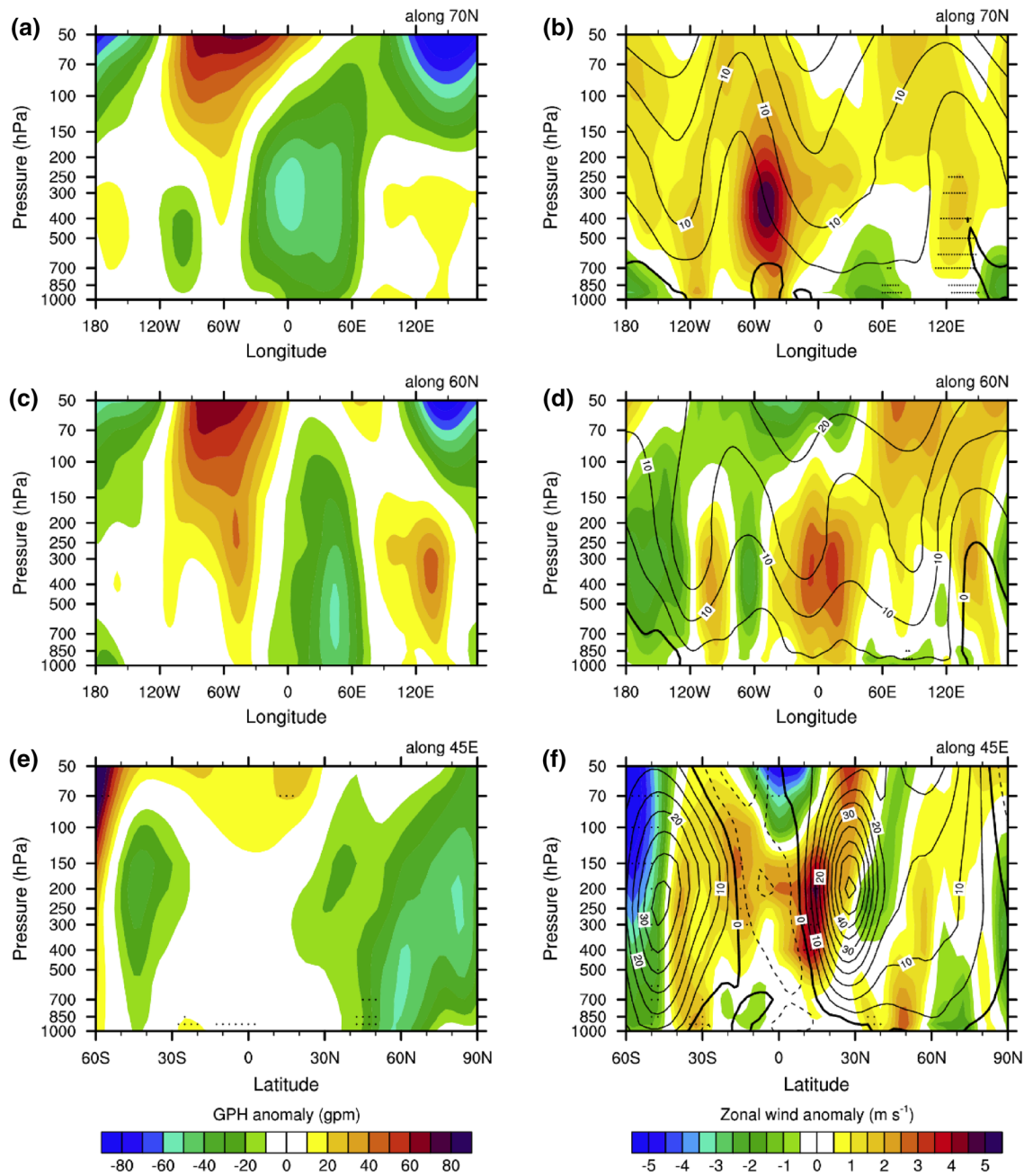


**Fig. 10** Cross sections of the differences between the composites of GPH anomaly (left panels) or zonal wind anomaly (right panels) **a, b** along the  $70^{\circ}$  N, **c, d** along the  $60^{\circ}$  N, **e, f** along the  $45^{\circ}$  E that during high TSI months and those during low TSI months (high minus low), respectively. **a, b, c, d** are pressure-longitude cross sections, **e, f** are pressure-latitude cross sections. The black contour lines in **b**,

**d, f** show the mean zonal wind of 180 samples (i.e., the climatological mean). The contour intervals are all  $5 \text{ m s}^{-1}$ , and ranges are **b, d**  $0\text{--}20 \text{ m s}^{-1}$ , **f**  $-10\text{--}50 \text{ m s}^{-1}$ . The thick black lines in **b, d, f** indicate  $0 \text{ m s}^{-1}$  contours, the negative contours in **f** are dashed. The dotted areas indicate the differences exceed the 95% confident level

region of Ural Mountains, where the region B ( $65^{\circ}\text{--}75^{\circ}$  N,  $45^{\circ}\text{--}60^{\circ}$  E) can be a key region for the interaction between the zonal flow and the Ural Mountains.

### 6.3 The mechanism of solar activity inducing the Ural circulation anomalies

Next, to investigate the mechanism of solar activity inducing the Ural circulation anomalies, we just need to investigate the mechanism of solar activity affecting the large-scale

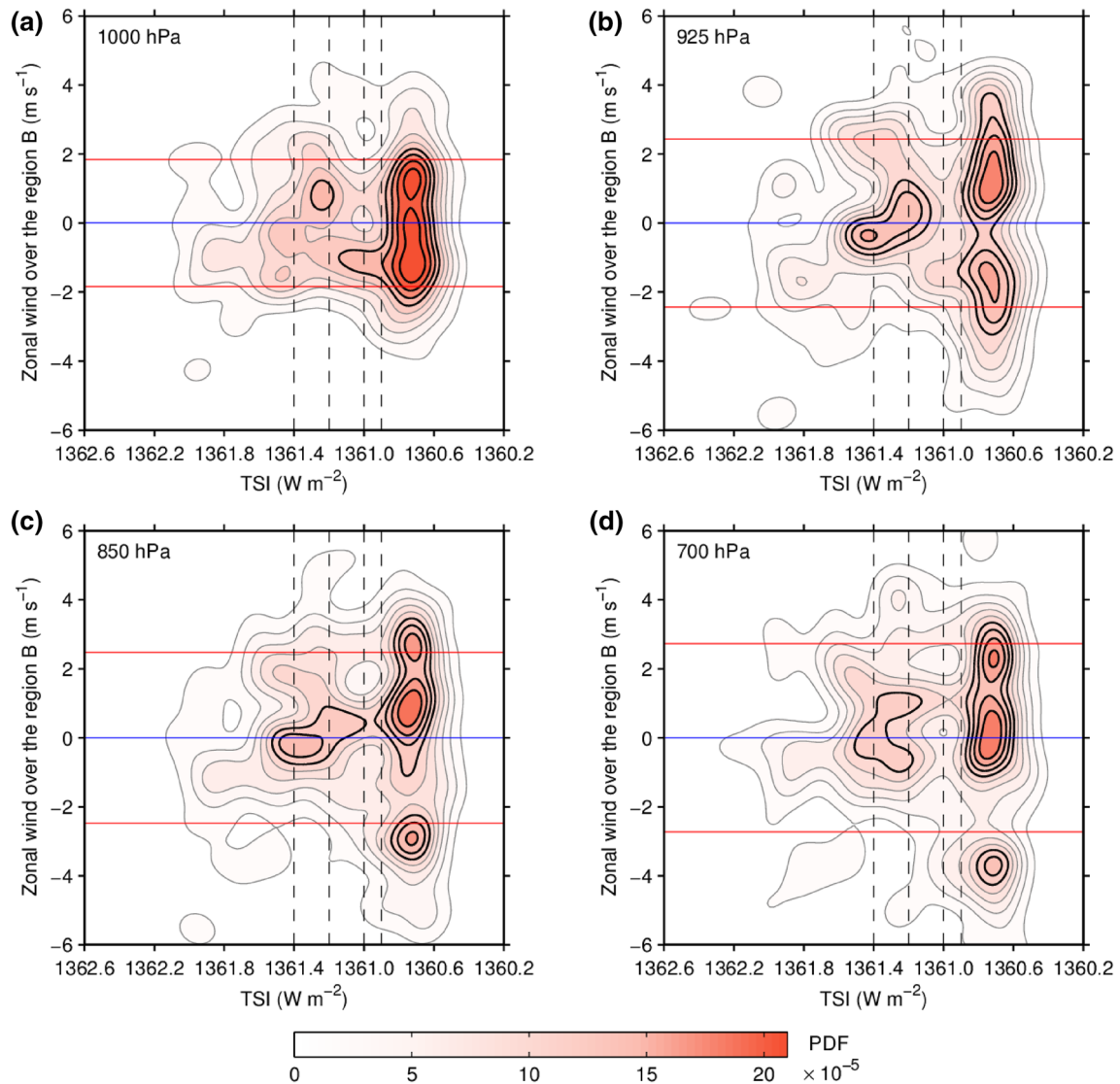


**Fig. 11** As in Fig. 6b, but for the joint PDFs of TSI and the area-averaged zonal wind over the region B **a** at 1000 hPa, **b** at 925 hPa, **c** at 850 hPa, **d** at 700 hPa. All of the zonal wind are deseasonalized.

Note that to retain the possible linear relationship between TSI and the zonal wind in the samples, the linear trends for all of the zonal wind should not be removed here

zonal flow in the lower-middle troposphere over the northern region of Ural Mountains.

Gray et al. (2010) summarized two categories of mechanism for solar influence on climate: the “bottom-up” and “top-down” mechanisms. The former suggests that changes in TSI can directly impact the surface, usually the ocean heat uptake and SST, hence affecting evaporation and atmospheric moisture. The latter suggests that the changes in ultraviolet irradiance can directly impact the stratosphere, then affecting the troposphere through stratosphere-troposphere coupling process.

Because what drives general circulation of the atmosphere is the thermal contrast at the Earth’s surface, Weng (2012) emphasized the changes in solar irradiance can

modify three kinds of thermal contrast: seasonal thermal contrast, equator-to-pole thermal contrast and land–ocean thermal contrast, thus affecting general circulation of the atmosphere and climate. These mechanisms belong to the “bottom-up” mechanism. The “seasonal thermal contrast” mechanism suggests that the Earth in the boreal winter is in the closest position to the sun over a year, thus, in the Northern Hemisphere, the general circulation in winter would be more sensitive to the change in the TSI than those in other seasons. The “equator-to-pole thermal contrast” mechanism suggests that because the high latitudes in winter are more sensitive to the change in TSI than the low latitudes, during the high (low) TSI, the high-latitudes surface receives more (less) solar radiation than normal,

while the low-latitudes surface does not change much, as a result, the equator-to-pole temperature gradient is reduced (increased), hence, the baroclinic ultra-long wave activity in mid-high latitudes is reduced (enhanced). The “land–ocean thermal contrast” mechanism suggests that because the land surface is more sensitive to the change in TSI than the ocean surface due to the different thermal inertia, during the high (low) TSI, the land surface temperature is warmer (colder) than normal, while the ocean surface temperature does not change much, as a result, the land–ocean thermal contrast is reduced (enhanced), hence, the stationary topographic waves are weakened (strengthened).

We next examine whether the mechanisms mentioned above are effective for our issue.

The cross sections of the differences between the composites of GPH anomaly and zonal wind anomaly during high TSI months and those during low TSI months (high minus low) are shown in Fig. 10. Compared with low TSI months, during high TSI months, there is negative GPH anomaly in the troposphere with equivalent barotropic structure around the Ural Mountains (ca. 60° E, Fig. 10a, c). Note that this negative GPH anomaly extends from the surface into the lower stratosphere, and the anomaly center is mainly in the troposphere, particularly, this negative GPH anomaly area is separable and independent from the other anomaly areas in the stratosphere, and for the latter, their anomaly centers are all in the upper stratosphere (Fig. 10a, c). In Fig. 10e, the negative GPH anomaly center around the Ural Mountains (ca. 60° N) extends from the surface to 400 hPa, this anomaly center is also separable from the anomaly area over the Arctic Pole, and for the latter, the GPH anomaly does not exist at the surface, and its anomaly center is confined to 200–300 hPa instead of the upper stratosphere. These results imply that the GPH anomaly in the troposphere around the Ural Mountains is unlikely to be induced by the GPH anomaly in the upper stratosphere through stratosphere–troposphere coupling process.

Besides, in Fig. 10b, d, f, the negative zonal wind anomaly around the Ural Mountains is also confined to the lower-middle troposphere, above this negative zonal wind anomaly area is the positive zonal wind anomaly area extending from the upper troposphere to the upper stratosphere, and the former is separable and independent from the latter. Thus, the negative zonal wind anomaly in the lower-middle troposphere over the Ural region is unlikely to be induced by the downward propagation of the positive zonal wind anomaly in the upper troposphere and the stratosphere.

It seems that the “top-down” mechanism associated with the stratosphere–troposphere coupling does not work for our issue. We next examine whether the “bottom-up” mechanism associated with the “equator-to-pole thermal contrast” and the “land–ocean thermal contrast” works or not for our issue.

Previous studies suggested that in the boreal winter, the increased TSI could give rise to the reduced Equator-to-Pole temperature gradient (e.g., Weng 2012; Soon and Legates 2013; Cai and Tung 2012) and the reduced land–ocean thermal contrast (e.g., Weng 2012; Chen et al. 2015). We next re-examine these conclusions.

We define the Equator-to-Pole temperature gradient index as the difference in surface temperature (at 1000 hPa) between the 0° and 20° N latitudinal band and the 70° and 90° N latitudinal band (low latitudes minus high latitudes). As shown in Fig. 12a, c, e, TSI shows decadal oscillation (known as quasi-11 years oscillation), while the Equator-to-Pole temperature gradient index shows interannual fluctuation, the correlation coefficients between these two time series are too small (not shown). If the two time series are smoothed by using the 9-year running mean method, it is seen that they have an out-of-phase relationship before 2000s (especially in December and January). After 2000s, the Equator-to-Pole temperature gradient index declines quickly, it can be attributed to the recent rapid Arctic warming which is known as “Arctic amplification” (e.g., Serreze et al. 2009; Francis and Vavrus 2012; Cohen et al. 2014). The correlation coefficients between the two smoothed time series during 1958–2017 are small, but that during 1958–2002 are –0.72 and –0.57 for December and January, respectively (significant at 95% confidence level). However, the corresponding correlation coefficient during 1958–2002 for February is still small. In addition, for the smoothed Equator-to-Pole temperature gradient index during 1958–2002, if the linear trends are removed, then corresponding correlation coefficients for December to February are –0.77, –0.69 and –0.40, respectively (significant at 95% confidence level for December and January, at 90% confidence level for February). It suggests that TSI and the Equator-to-Pole temperature gradient index have an out-of-phase relationship before 2000s in decadal time scale. It also suggests that the recent Arctic warming has an important influence on the Equator-to-Pole thermal contrast, and this issue will be discussed in Sect. 7.1.

In boreal winter, the Eurasia and North America are colder than the North Atlantic and North Pacific in mid-high latitudes (Fig. 9e, see the 0 °C contour). Compared with low TSI months, during high TSI months, there is strong warm anomaly center over the Ural region, while the surface temperature over the North Atlantic does not change much (Fig. 9e, see shaded area). We define the Land–Sea index as the area-averaged surface temperature (at 1000 hPa) difference between the region (30°–50° N, 40°–10° W) over the North Atlantic and the region (30°–50° N, 45°–75° E) over the south of Ural Mountains (the former minus the latter; see two blue boxes in Fig. 9e). It's seen that the smoothed time series of TSI and the Land–Sea index show an apparent out-of-phase relationship (Fig. 12b, d, f), the correlation

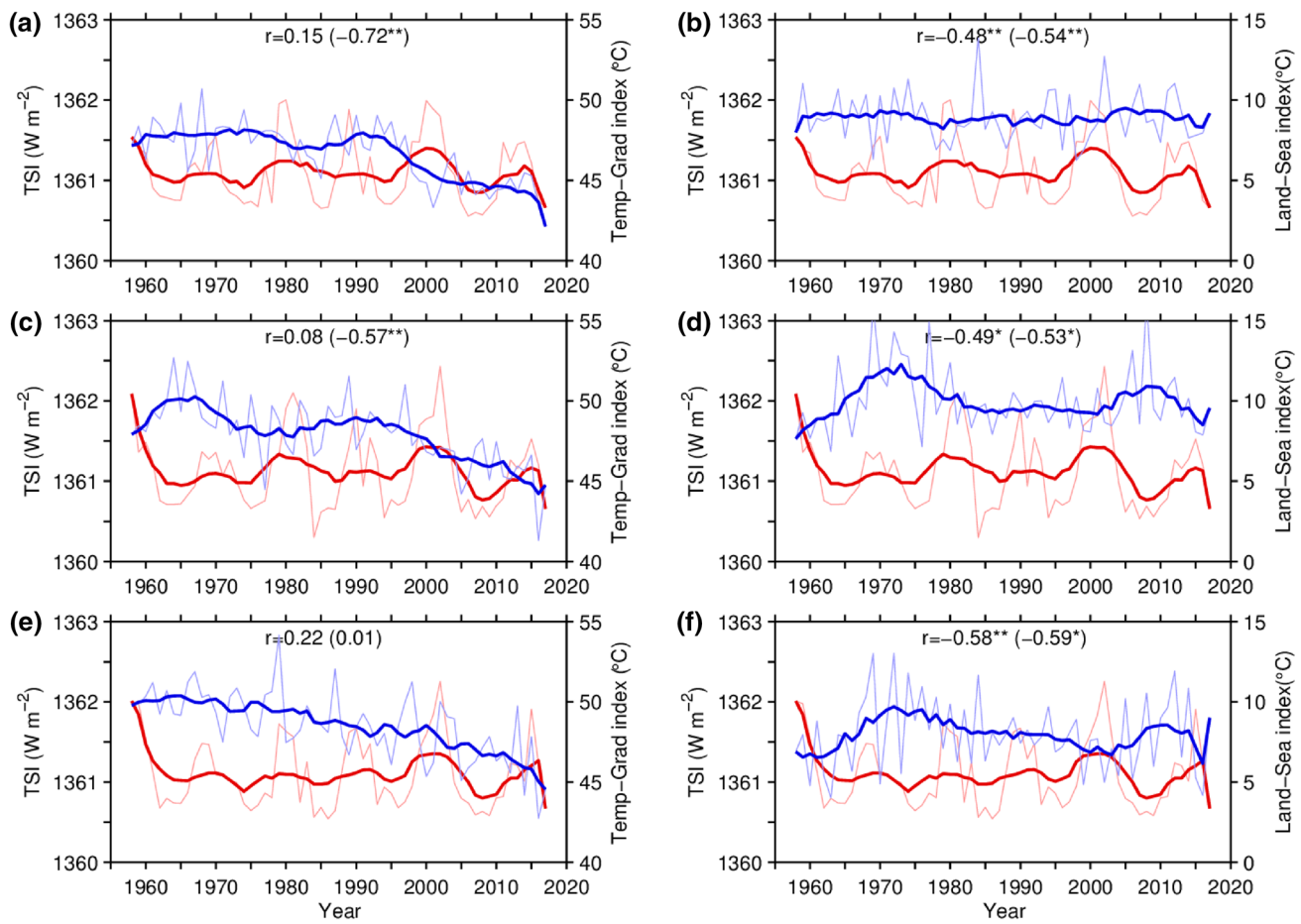


**Fig. 12** Time series of TSI (thin red lines) and **a, c, e** the Equator-to-Pole temperature gradient index, **b, d, f** the Land-Sea index during winter 1958–2017 for **a, b** December, **c, d** January and **e, f** February, respectively. The thick lines indicate 9-year running mean values. The correlation coefficient  $r$  between TSI and the corresponding variable

is given for the smoothed time series during 1958–2017 and 1958–2002 (shown in the bracket). For two-sided Student's t test, the effective sample size is used, the superscript “\*” and “\*\*” indicate that the correlation coefficient is significant at 90% and 95% confidence level, respectively

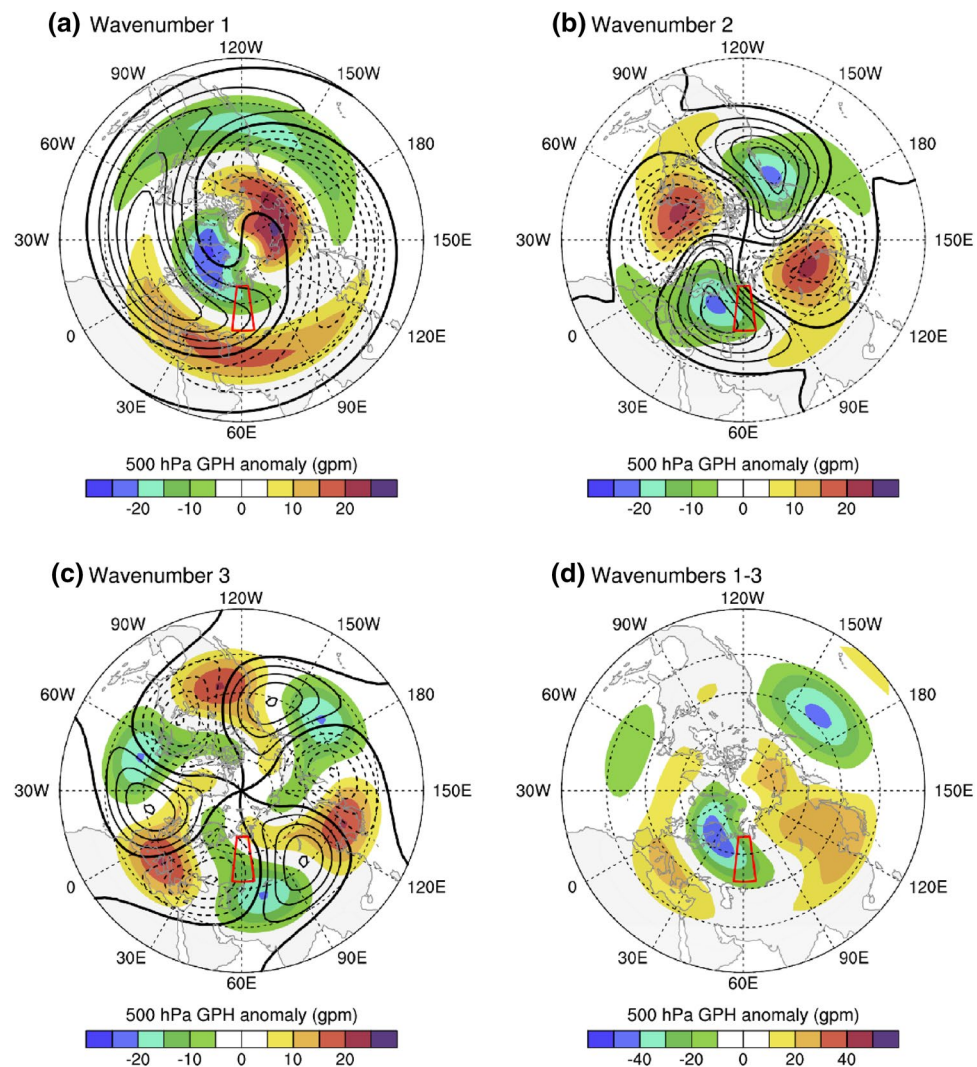
coefficients between them during 1958–2017 (1958–2002) are  $-0.48$ ,  $-0.49$  and  $-0.58$  ( $-0.54$ ,  $-0.53$  and  $-0.59$ ) for December to February, respectively (significant at 95% or 90% confidence level). The correlation coefficients between the original time series of TSI and the Land-Sea index are too small (not shown).

Therefore, the high (low) TSI is corresponding to the reduced (enhanced) Equator-to-Pole and Land–Ocean thermal contrast. According to Weng (2012), the ultra-long wave activity in mid-high latitudes should be reduced (enhanced) during high (low) TSI. Figure 13 shows the differences between the composites of GPH anomaly at 500 hPa with different zonal wave components that during high TSI months and those during low TSI months. In general, the zonal wavenumber 1, 2 and 3 planetary waves are quasi-stationary. Compared with low TSI months, during high TSI months, the zonal wavenumber-1 wave is weaker than normal in high latitudes and shifts eastward in middle latitudes

(Fig. 13a), the zonal wavenumber-2 wave is also weaker than normal (Fig. 13b), the zonal wavenumber-3 wave also shifts eastward (Fig. 13c). The sum of these three quasi-stationary planetary wave components shows a spatial pattern (Fig. 13d) resembling that shown in Fig. 9a. Note that the strengthened European trough in Fig. 9a is mainly attributed to the weakened zonal wavenumber 1 and 2 planetary waves in mid-high latitudes.

In summary, how the solar activity induces the atmospheric circulation anomalies over the Ural Mountains in boreal winter can be described in Fig. 14 as a schematic diagram. In general, during high (low) TSI months, the Equator-to-Pole thermal contrast and the Land–Ocean thermal contrast are both reduced (enhanced) (Fig. 12), thus, the quasi-stationary planetary waves in mid-high latitudes is weakening (strengthening) and/or shifts eastward (westward) (Fig. 13). As a result, the European trough is strengthening (weakening) (Fig. 9a), the corresponding change in the

**Fig. 13** The differences between the composites of GPH anomaly at 500 hPa with the **a** zonal wavenumber-1 component, **b** zonal wavenumber-2 component, **c** zonal wavenumber-3 component, **d** the sum of zonal wavenumbers 1, 2 and 3 components that during high TSI months and those during low TSI months (high minus low), respectively. The black contour lines in **a**, **b**, **c** show the mean of 180 samples (i.e., the climatological mean) for the GPH with corresponding zonal wave components. The contour intervals and ranges are all 20 gpm and  $-80$  to  $80$  gpm, the thick black lines indicate 0 gpm contours, the negative contours are dashed. Red boxes enclose the region of Ural Mountains



horizontal pressure gradient leads to a weakening (strengthening) in the large-scale zonal flow (i.e., westerlies) in the lower-middle troposphere over the northern region of Ural Mountains, e.g., the region B (Figs. 9, 10). The zonal wind at 925 hPa over the region B can be an indicator of the solar activity affecting Ural circulation anomalies, and  $1360.9 \text{ W m}^{-2}$  can be a critical value of TSI. Whether single or duplex circulation regimes occur depend on the interaction between the large-scale zonal flow and the Ural Mountains:

- When the TSI is above the critical value  $1360.9 \text{ W m}^{-2}$ , as affected by the solar activity, the zonal wind at 925 hPa over the region B would be below the “critical velocity” of the bifurcation, thus, the large-scale zonal flow would do not interact with the Ural Mountains. In this case, as the TSI decreases, the zonal wind at 925 hPa tends to increase (Fig. 11b), in other word, the TSI and the zonal wind at 925 hPa tend to have a one-to-

one relationship. Therefore, the neutral type pattern as a single circulation regime is observed around the Ural Mountains (Figs. 8c, f, g, 11b).

- When the TSI is below the critical value  $1360.9 \text{ W m}^{-2}$ , as affected by the solar activity, the zonal wind at 925 hPa over the region B would be beyond the “critical velocity” of the bifurcation, thus, the large-scale zonal flow would interact with the Ural Mountains. In this case, the supercritical pitchfork bifurcation would occur, i.e., either the trough anomaly or ridge anomaly would occur. As a result, the zonal wind at 925 hPa tends to be either less than or greater than the climatological mean value (Fig. 11b), in other word, the TSI and the zonal wind at 925 hPa tend to have a one-to-two relationship. Therefore, the trough anomaly and ridge anomaly patterns as the duplex circulation regimes are observed around the Ural Mountains (Figs. 8c, f, g, 11b).

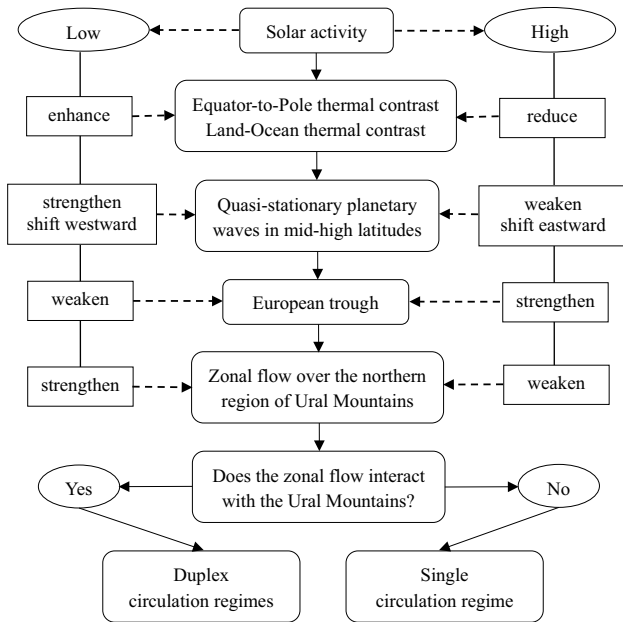


**Fig. 14** Schematic diagram of solar activity affecting the atmospheric circulation anomalies over the Ural Mountains in boreal winter

Note that although the zonal wind at 925 hPa over the region B can be an indicator of the solar activity affecting Ural circulation anomalies, it is hard for us to find the “critical velocity” of the bifurcation, due to the complexity of atmospheric circulation. Nevertheless,  $1360.9 \text{ W m}^{-2}$  as a critical value of TSI is a good indicator of the bifurcation.

## 7 Discussion

### 7.1 The influence of other factors on Ural atmospheric circulation

In fact, besides the solar activity, many other factors can affect the Ural atmospheric circulation. As typical examples, we next briefly discuss the influences of the Arctic warming, Arctic sea ice, the Equator-to-Pole and Land–Ocean thermal contrast, and the Northern Hemisphere Annular Mode.

The rapid Arctic warming gives rise to the decline in the temperature gradient between the mid-latitudes and the Arctic (e.g., Francis and Vavrus 2012; Cohen et al. 2014), as well as the decrease in the Equator-to-Pole temperature gradient (Fig. 12a, c, e). In Fig. 12, for the smoothed time series, the correlation coefficients between TSI and the corresponding variable are higher during 1958–2002 than those during 1958–2017, it implies the recent Arctic warming has important influences on the Ural atmospheric circulation and the horizontal thermal gradient at the Earth’s surface. To exclude the influences of Arctic warming on our results, on the one hand, the seasonal cycle signals and long-term trends

in the samples have been removed for the Z and U indices (Figs. 6c, d, 8b, c, f, g), on the other hand, the samples after 2002 are also removed (see Fig. 15a), in these cases, the joint PDFs of TSI and the Z/U index still show apparent trident-like or two-tine-pitchfork-like patterns (Figs. 6c, d, 8b, c, f, g, 15a). Thus, the influence of the Arctic warming on our results is negligible.

Moreover, many studies reported that the rapid surface warming and sea ice decline over the Barents-Kara Sea (BK) have important influences on the extreme weather and climate in mid-latitudes (e.g., Wu et al. 1999; Honda et al. 2009; Petoukhov and Semenov 2010; Mori et al. 2014). To explore the influences of surface warming and sea ice decline over BK on Ural atmospheric circulation, we define the BK temperature index as the area-averaged surface temperature (at 1000 hPa) over the BK region ( $70^{\circ}\text{--}80^{\circ}\text{N}$ ,  $40^{\circ}\text{--}80^{\circ}\text{E}$ ), and the BK sea ice index is defined as the area-averaged sea ice concentration over the same BK region (the time series of these two indices are shown in Supplementary Fig. S3). The joint PDFs of the BK temperature index and the Z index, as well as the BK sea ice index and the Z index, both do not show a pitchfork-like pattern (Fig. 15b, c). It’s seen that when the BK surface is relatively cold (the BK temperature index is below  $-15^{\circ}\text{C}$ ) and the BK sea ice concentration is relatively high (the BK sea ice index is above 0.6), the neutral type pattern is the most dominant circulation pattern. By contrast, when the BK surface is too warm (the BK temperature index is above  $-10^{\circ}\text{C}$ ) and the BK sea ice concentration is too low (the BK sea ice index is below 0.4), the strong ridge anomaly pattern tends to occur frequently.

We have demonstrated in Sect. 6 that the solar activity affects the Ural atmospheric circulation through changes in the Equator-to-Pole and the Land–Ocean thermal contrast. In fact, besides the solar activity, the Equator-to-Pole and the Land–Ocean thermal contrast can be affected by many other factors, such as the Arctic sea ice decline and the Arctic warming (e.g., Honda et al. 2009; Petoukhov and Semenov 2010; Francis and Vavrus 2012; Cohen et al. 2014), the greenhouse gas and the global warming (e.g., Sutton et al. 2007; Dong et al. 2009; He et al. 2014, 2018) and the internal climate variability (e.g., Huang et al. 2017). Thus, it is necessary to directly investigate the relationships between the Equator-to-Pole and the Land–Ocean thermal contrast and the Ural atmospheric circulation. As shown in Fig. 15d, e, the joint PDFs of the Equator-to-Pole temperature gradient index and the Z index, as well as the Land–Ocean index and the Z index, both do not show a pitchfork-like pattern. It’s seen that the PDF peak regions in Fig. 15d, e both represent the neutral type and the trough anomaly patterns.

According to the physical mechanism we proposed in Sect. 6, besides the solar activity, as long as other factors (e.g., Arctic warming, Arctic sea ice, the Equator-to-Pole

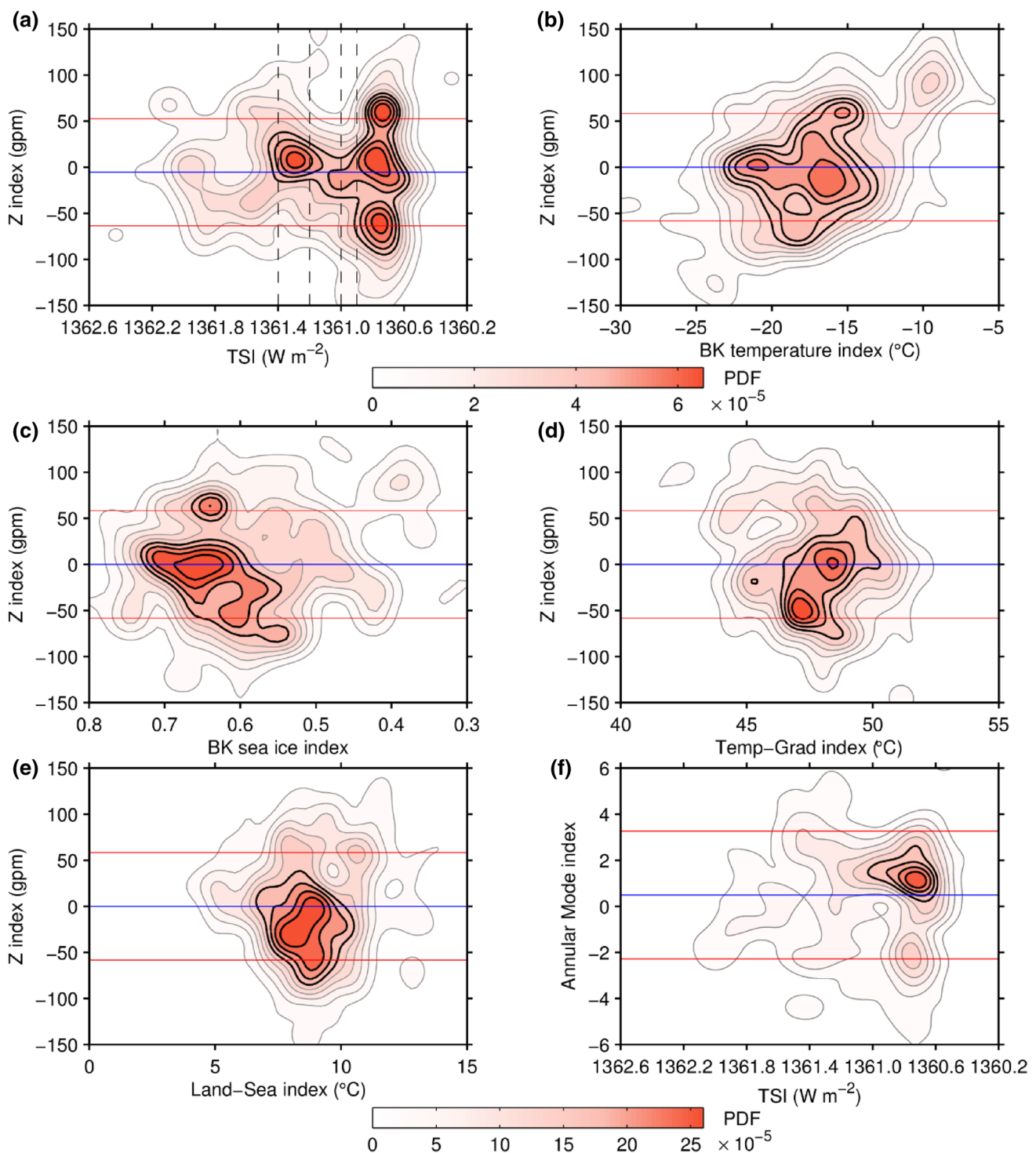


**Fig. 15** **a** As in Fig. 6c, but for 135 samples during winter 1958–2002. As in Fig. 6c, but for the joint PDFs of the deseasonalized and detrended Z index and **b** the BK temperature index, **c** the BK sea ice index, **d** the Equator-to-Pole temperature gradient index, **e** the Land–Sea index. **f** As in Fig. 6c, but for the joint PDF of TSI and the Northern Hemisphere Annular Mode index. The BK temperature index, the

BK sea ice index, the Temp-Grad index, the Land-Sea index and the Annular Mode index are partitioned with a bin width of 0.1  $^{\circ}\text{C}$ , 0.01, 0.2  $^{\circ}\text{C}$ , 0.2  $^{\circ}\text{C}$  and 0.1 for the joint probability density estimates, with the bandwidths of smoothing window of 1.0  $^{\circ}\text{C}$ , 0.02, 0.5  $^{\circ}\text{C}$ , 0.5  $^{\circ}\text{C}$  and 0.5

and Land–Ocean thermal contrast) can affect the large scale zonal flow over the Ural Mountains, the supercritical pitchfork bifurcation phenomena should also occur. Why do Fig. 15b–e not show a pitchfork-like pattern? The possible reason may be that the BK surface temperature, the BK sea ice, the Equator-to-Pole and the Land–Ocean thermal contrast are not the external forcing for the atmospheric circulation, that is, they can determine the general circulation, but they can also be affected by the atmospheric circulation through some feedback processes. For example, the Ural atmospheric circulation can directly affect the surface temperature and sea ice over BK though the heat transport (Fig. 2c–f). By contrast, the solar activity is an external forcing for the atmospheric circulation, it cannot be affected by the Earth's atmosphere. In fact, L18 also showed the relationship between the meridional temperature gradient and the channel-averaged zonal wind at the lower layer in the model, and the relationship does not follow the supercritical pitchfork bifurcation theory (see Supplementary Fig. S4), because the meridional temperature gradient is not an external forcing.

The Northern Hemisphere Annular Mode or Arctic Oscillation is a hemispheric scale pattern of circulation variability, characterized by the fluctuations in air pressure occurring between the mid- and high-latitude annular belt of actions (Thompson and Wallace 1998, 2000; Li and Wang 2003). During the positive (negative) phase of the Annular Mode, surface westerlies in mid-high latitudes are stronger (weaker) than normal (e.g., Li and Wang 2003). The correlation coefficients between the Northern Hemisphere Annular Mode index and the U index during 1958–2017 are 0.36, 0.62 and 0.39 for December to February, respectively (significant at 95% confidence level). If the two time series are smoothed by using the 9-year running mean method, the corresponding correlation coefficients are 0.73, 0.77 and 0.57 for December to February, respectively (significant at 90% confidence level for December, at 95% confidence level for January and February). It suggests that to a considerable degree, the U index partly represents the circulation variability of the Northern Hemisphere Annular Mode. Thus, it is interesting to examine whether the joint PDF of TSI and the Annular Mode index shows a pitchfork-like pattern. However, as shown in Fig. 15f, the joint PDF shows only one peak region. Thus, the trident-like or two-tine-pitchfork-like patterns shown in Figs. 6 and 8b, c, f, g cannot be attributed to the circulation variability.

In a word, the results above suggest that the occurrence of the trident-like or two-tine-pitchfork-like patterns in the joint PDFs of TSI and the Z/U indices (Figs. 6, 8b, c, f, g) cannot be optionally ascribed to the influences of other factors.

## 7.2 Uncertainty of the reconstructed TSI

Throughout our statistical analyses, we use the reconstructed TSI values instead of the measured TSI values, because the time period covered by the TSI measurements is too short. However, compared with the measured TSI values, the reconstructed TSI values are systematically overestimated (Fig. 16a–c). In addition, the PDFs of measured and reconstructed TSI values during winter 1979–2017 both show a dominant peak and a sub-peak (Fig. 16e). However, compared with the PDF of measured TSI, the PDF of reconstructed TSI is right-shifted, also suggesting the reconstructed TSI values are systematically overestimated. Besides, the reconstructed TSI shows a higher dominant PDF peak, suggesting the reconstructed TSI values are somewhat more concentrated. Thus, results based on the reconstructed TSI values should have a certain degree of uncertainty, particularly, it suggests that the  $1360.9 \text{ W m}^{-2}$  as a critical value of TSI should be overestimated.

Nevertheless, by using the reconstructed TSI values, not only the joint PDFs of TSI and the Z/U index (Figs. 6, 8b, c, f, g), but also the frequencies of occurrence for trough and ridge anomaly events (Fig. 7, Table 1) generally agree with the theoretical model (Fig. 4), these results do not seem to be coincidental and accidental. Moreover, note that the joint PDF peak regions generally exist during the TSI range  $1360.6\text{--}1361.4 \text{ W m}^{-2}$ , particularly the two TSI ranges:  $1360.6\text{--}1360.9 \text{ W m}^{-2}$  and  $1361.1\text{--}1361.4 \text{ W m}^{-2}$  (Figs. 6, 8b, c, f, g), the PDF of the reconstructed TSI also shows high values during the same TSI ranges (Fig. 16d). Thus, within these TSI ranges, the sample sizes are sufficient. In short, our results based on the reconstructed TSI values should be reliable.

## 7.3 Strong trough and ridge anomaly patterns

People may be more interested in the strong trough/ridge anomaly patterns than the weak trough/ridge anomaly and the neutral type patterns, because the strong trough/ridge anomaly patterns have higher impacts on the regional weather and climate. We next have a brief discussion on the strong trough/ridge anomaly patterns.

Figures 5c, d and 6 all show the strong trough and ridge anomaly patterns over the Ural Mountains are both circulation regimes or preferred circulation patterns. Moreover, Fig. 6 shows there are two joint PDF peak regions that represent the strong trough and ridge anomaly patterns when  $\text{TSI} \leq 1360.9 \text{ W m}^{-2}$ , suggesting the strong trough/ridge anomaly events prefer to occur during relatively low TSI. According to Table 1, for the 180 samples, the total strong trough/ridge anomaly events are 55 (58) based on the Z (U) index, among them 28 events occur during  $\text{TSI} \leq 1360.9 \text{ W m}^{-2}$ . Thus, 51% (48%) strong trough/

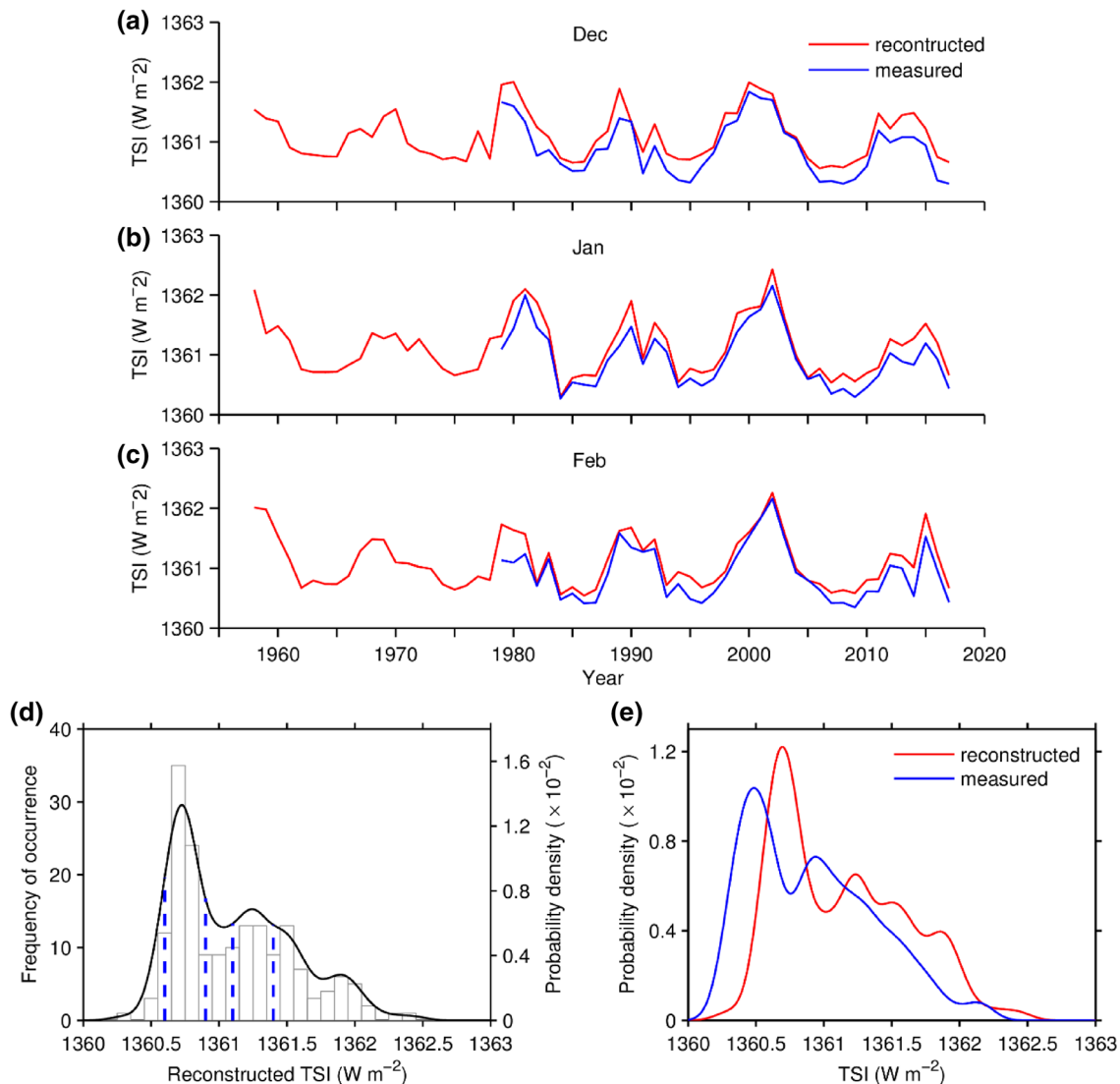


**Fig. 16** TSI time series for **a** December, **b** January, **c** February, respectively. The reconstructed TSI time series (red lines) covers the time period of 1958–2017, while the measured TSI times series (blue lines) covers the time period of 1979–2017. **d** Histogram (thin bars) and PDF (thick curves) of reconstructed TSI during winter 1958–2017. **e** The PDFs of measured and reconstructed TSI during winter

1979–2017. The TSI is partitioned with a bin width of  $0.01 \text{ W m}^{-2}$  for probability density estimates, with a bandwidth of smoothing window of  $0.1 \text{ W m}^{-2}$ . The bin width for histogram estimates of TSI is  $0.1 \text{ W m}^{-2}$  in **d**. Four vertical blue dashed lines in **d** indicate that TSI is equal to  $1360.6$ ,  $1360.9$ ,  $1361.1$  and  $1361.4 \text{ W m}^{-2}$ , respectively

ridge anomaly events occur during  $\text{TSI} \leq 1360.9 \text{ W m}^{-2}$  based on the Z (U) index. Because the  $1360.9 \text{ W m}^{-2}$  can be a critical value (or bifurcation point) of TSI, to some extent, it indicates the “supercritical pitchfork bifurcation theory” accounts for about 50% strong trough/ridge anomaly events over the Ural Mountains in boreal winter, it also suggests that the solar activity is an important driving factor for the occurrence of the strong trough/ridge anomaly events.

## 8 Conclusions

In this paper, guided by a simple theoretical model associated with the supercritical pitchfork bifurcation theory, we have explored the nonlinear relationship between TSI and monthly mean atmospheric circulation over the Ural Mountains. We find that there is an analogy between the anomalies of Ural atmospheric circulation and the

buckling of a vertical elastic rod, where the latter is a typical example of the supercritical pitchfork bifurcation. The neutral type, trough anomaly and ridge anomaly patterns over the Ural Mountains under the solar forcing are analogous to the non-buckling, left-side buckling and right-side buckling, respectively, of a vertical elastic rod under an axial load. The results of our statistical analyses generally agree with those of the theoretical model:

1. The three main peaks in the PDFs of Z and U indices (Fig. 5) indicate that the three Ural circulation patterns are all circulation regimes or preferred circulation patterns. Particularly,  $S_c = 1360.9 \text{ W m}^{-2}$  is a critical value of TSI, the neutral type pattern is the single circulation regime when  $\text{TSI} > S_c$ ; By contrast, the trough anomaly and ridge anomaly patterns are duplex circulation regimes when  $\text{TSI} < S_c$  (Figs. 8c, f, g, 11b). Similarly, when the axial load is below the critical value, the non-buckling is the single equilibrium state of the vertical elastic rod; By contrast, when the axial load is beyond the critical value, the left-side buckling and right-side buckling are duplex equilibrium states of the vertical elastic rod (Fig. 4c, d).
2. When the TSI is below the critical value  $S_c = 1360.9 \text{ W m}^{-2}$ , during the same TSI range, the frequencies of occurrence for the trough anomaly and ridge anomaly events are almost equal to each other (Table 1, Table S1, Fig. 7). Just like under an axial load which is beyond the critical value, the left-side buckling and right-side buckling of the vertical elastic rod are equally likely to occur.

Therefore, when TSI is below  $1360.9 \text{ W m}^{-2}$ , the trough anomaly and ridge anomaly patterns, which are two basic types of Ural circulation anomalies, can be considered duplex equilibria at the same TSI, and they should be equally likely to occur at the same TSI. Moreover, the “supercritical pitchfork bifurcation theory” accounts for about 50% strong trough/ridge anomaly events over the Ural Mountains in boreal winter. To some extent, the relationship between TSI and trough/ridge anomaly events over the Ural Mountains is a one-to-two relationship following the supercritical pitchfork bifurcation theory. The physical mechanism of solar activity inducing Ural circulation anomalies is proposed in Sect. 6 and summarized by a schematic diagram in Fig. 14. Compared to most previous studies on the relationships between solar activity and atmospheric circulation anomalies, our findings are innovative.

However, according to the findings in this paper, it remains difficult to predict which circulation pattern will occur during most TSI ranges. On the one hand, the trough anomaly and ridge anomaly events should be equally likely to occur when  $\text{TSI} \leq 1360.9 \text{ W m}^{-2}$ , thus, whether a trough

anomaly or ridge anomaly event will occur is unknown. On the other hand, only half (51% or 48%) of the strong trough/ridge anomaly events occur during  $\text{TSI} \leq 1360.9 \text{ W m}^{-2}$ , thus, whether the strong trough/ridge anomaly events will occur during  $\text{TSI} \leq 1360.9 \text{ W m}^{-2}$  or  $\text{TSI} > 1360.9 \text{ W m}^{-2}$  is unknown. Apparently, solar activity is not the only one forcing factor, the observed Ural circulation anomalies have been affected by many other forcing factors (e.g., Eurasian snow cover, Arctic sea ice, and Atlantic sea surface temperature). It's unsurprising that the simple theoretical model used in this study could not fully elucidate the mechanism of Ural circulation anomalies.

Overall, in this study, we provide a new perspective on the mechanism of solar influence on atmospheric circulation anomalies over the Ural Mountains. Our findings are preliminary and enlightening. Studies include determining reliable precursors for Ural circulation anomalies, the transitions between Ural circulation patterns, and the dynamics of strong trough and ridge anomaly patterns should be undertaken in the future.

**Acknowledgements** The authors appreciate three anonymous reviewers for their detailed comments and constructive suggestions, which helped to improve the paper. This work was jointly supported by the National Science Foundation of China (41521004 and 41705047), the Strategic Priority Research Program of Chinese Academy of Sciences, Grant no. XDA2006010301 and the Foundation of Key Laboratory for Semi-Arid Climate Change of the Ministry of Education in Lanzhou University from the Fundamental Research Funds for the Central Universities (lzjbky-2017-bt04) and the China 111 project (no. B13045).

## References

- Afyouni S, Smith SM, Nichols TE (2019) Effective degrees of freedom of the Pearson's correlation coefficient under autocorrelation. *NeuroImage* 199:609–625
- Barriopedro D, Garcia-Herrera R, Huth R (2008) Solar modulation of Northern Hemisphere winter blocking. *J Geophys Res* 113:D14118. <https://doi.org/10.1029/2008jd009789>
- Cai M, Tung KK (2012) Robustness of dynamical feedbacks from radiative forcing: 2% solar versus  $2 \times \text{CO}_2$  experiments in an idealized GCM. *J Atmos Sci* 69:2256–2271. <https://doi.org/10.1175/jas-d-11-0117.1>
- Chen HS, Ma HD, Li X, Sun SL (2015) Solar influences on spatial patterns of Eurasian winter temperature and atmospheric general circulation anomalies. *J Geophys Res Atmos* 120:8642–8657. <https://doi.org/10.1002/2015jd023415>
- Chen SF, Wu RG, Chen W, Yao SL (2018) Enhanced linkage between Eurasian winter and Spring dominant modes of atmospheric interannual variability since the early 1990s. *J Clim* 31:3575–3595. <https://doi.org/10.1175/jcli-d-17-0525.1>
- Cheung HHN, Zhou W (2016) Simple metrics for representing East Asian winter monsoon variability: Urals blocking and western Pacific teleconnection patterns. *Adv Atmos Sci* 33(6):695–705. <https://doi.org/10.1007/s00376-015-5204-6>
- Cheung HHN, Zhou W, Mok HY, Wu MC (2012) Relationship between Ural-Siberian blocking and the East Asian winter monsoon in relation to the Arctic Oscillation and the El Nino-Southern

- Oscillation. *J Clim* 25:4242–4257. <https://doi.org/10.1175/jcli-d-11-00225.1>
- Christiansen B (2005) Bimodality of the planetary-scale atmospheric wave amplitude index. *J Atmos Sci* 62:2528–2541
- Coddington O, Lean J (2015) Climate algorithm theoretical basis document (C-ATBD): total solar irradiance and solar spectral irradiance. CRDP-ATBD-0612, NOAA/NCDC
- Cohen J, Screen JA, Furtado JC, Barlow M, Whittleston D et al (2014) Recent Arctic amplification and extreme mid-latitude weather. *Nat Geosci* 7:627–637. <https://doi.org/10.1038/NGEO2234>
- Dijkstra HA (2013) Nonlinear climate dynamics. Cambridge University Press, Cambridge
- Ding YH (1994) Monsoon over China. Kluwer Academic Publishers, Groningen
- Ding YH, Chan JCL (2005) The East Asian summer monsoon: an overview. *Meteorol Atmos Phys* 89:117–142. <https://doi.org/10.1007/s00703-005-0125-z>
- Dole RM, Gordon ND (1983) Persistent anomalies of the extratropical Northern Hemisphere wintertime circulation: geographical distribution and regional persistence characteristics. *Mon Weather Rev* 111:1567–1586
- Dong BW, Gregory JM, Sutton RT (2009) Understanding land-sea warming contrast in response to increasing greenhouse gases. Part I: Transient adjustment. *J Clim* 22:3079–3097. <https://doi.org/10.1175/2009jcli2652.1>
- Emerson JD, Hoaglin DC (1983) Stem-and-leaf displays. In: Hoaglin DC, Mosteller F, Tukey JW (eds) Understanding robust and explanatory data analysis. Wiley, New York, pp 7–32
- Francis JA, Vavrus SJ (2012) Evidence linking Arctic amplification to extreme weather in mid-latitudes. *Geophys Res Lett* 39:L06801. <https://doi.org/10.1029/2012gl051000>
- Fröhlich C (2006) Solar irradiance variability since 1978: revision of the PMOD composite during solar cycle 21. *Sp Sci Rev* 125:53–65. <https://doi.org/10.1007/s11214-006-9046-5>
- Gray LJ, Beer J, Geller M, Haigh JD, Lockwood M et al (2010) Solar influences on climate. *Rev Geophys* 48:RG4001. <https://doi.org/10.1029/2009rg000282>
- Gray LJ, Woollings TJ, Andrews M, Knight J (2016) Eleven-year solar cycle signal in the NAO and Atlantic/European blocking. *Q J R Meteorol Soc* 142:1890–1903. <https://doi.org/10.1002/qj.2782>
- Han SZ, Sun JQ (2018) Impact of autumnal Eurasian snow cover on predominant modes of boreal winter surface air temperature over Eurasia. *J Geophys Res Atmos* 123:10076–10091. <https://doi.org/10.1029/2018jd028443>
- Han Z, Li SL, Mu M (2011) The role of warm North Atlantic SST in the formation of positive height anomalies over the Ural Mountains during January 2008. *Adv Atmos Sci* 28(2):246–256. <https://doi.org/10.1007/s00376-010-0069-1>
- Hannachi A, Straus DM, Franzke CLE, Corti S, Woollings T (2017) Low frequency nonlinearity and regime behavior in the Northern Hemisphere extratropical atmosphere. *Rev Geophys* 55:199–234. <https://doi.org/10.1002/2015rg000509>
- Hansen A, Sutera A (1986) On the probability density distribution of planetary-scale atmospheric wave amplitude. *J Atmos Sci* 43(24):3250–3265
- He YL, Huang JP, Ji MX (2014) Impact of land-sea thermal contrast on interdecadal variation in circulation and blocking. *Clim Dyn* 43:3267–3279. <https://doi.org/10.1007/s00382-014-2103-y>
- He YL, Huang JP, Li DD, Xie YK, Zhang GL et al (2018) Comparison of the effect of land-sea thermal contrast on interdecadal variations in winter and summer blockings. *Clim Dyn* 51:1275–1294. <https://doi.org/10.1007/s00382-017-3954-9>
- Honda M, Inoue J, Yamane S (2009) Influence of low Arctic sea-ice minima on anomalously cold Eurasian winters. *Geophys Res Lett* 36:L08707. <https://doi.org/10.1029/2008gl037079>
- Huang JP, Xie YK, Guan XD, Li DD, Ji F (2017) The dynamics of the warming hiatus over the Northern Hemisphere. *Clim Dyn* 48:429–446. <https://doi.org/10.1007/s00382-016-3085-8>
- Huth R, Kyselý J, Bochníček J, Hejda P (2008) Solar activity affects the occurrence of synoptic types over Europe. *Ann Geophys* 26:1999–2004. <https://doi.org/10.5194/angeo-26-1999>
- Ineson S, Scaife AA, Knight JR, Manners JC, Dunstone NJ, Gray LJ, Haigh JD (2011) Solar forcing of winter climate variability in the Northern Hemisphere. *Nat Geosci* 9:753–757. <https://doi.org/10.1038/ngeo1282>
- Kalnay E, Kanamitsu M, Kistler R, Collins W, Deaven D et al (1996) The NCEP/NCAR 40-year reanalysis project. *Bull Am Meteorol Soc* 77(3):437–470
- Kobayashi S, Ota Y, Harada Y, Ebita A, Moriya M et al (2015) The JRA-55 reanalysis: general specifications and basic characteristics. *J Meteorol Soc Japan* 93(1):5–48. <https://doi.org/10.2151/jmsj.2015-001>
- Kodera K (2003) Solar influence on the spatial structure of the NAO during the winter 1900–1999. *Geophys Res Lett* 30(4):1175. <https://doi.org/10.1029/2002gl016584>
- Kuroda Y, Kodera K (2005) Solar cycle modulation of the Southern Annular Mode. *Geophys Res Lett* 32:L13802. <https://doi.org/10.1029/2005gl022516>
- Lee JN, Hameed S (2007) Northern Hemisphere annular mode in summer: its physical significance and its relation to solar activity variations. *J Geophys Res* 112:D15111. <https://doi.org/10.1029/2007jd008394>
- Li SL (2004) Impact of Northwest Atlantic SST anomalies on the circulation over the Ural Mountains during early winter. *J Meteorol Soc Jpn* 82(4):971–2004
- Li JL, Ji LR (1994) Geographical distribution and regional characteristics of 500 hPa height persistent anomalies during Northern Hemisphere summertime. *Sci Atmos Sin* 18(2):163–172 (in Chinese)
- Li SL, Ji LR (2001) Persistent anomaly in Ural area in summer and its background circulation characteristics. *Acta Meteorol Sin* 59(3):280–293 (in Chinese)
- Li JP, Wang JXL (2003) A modified zonal index and its physical sense. *Geophys Res Lett* 30(12):1632. <https://doi.org/10.1029/2003gl017441>
- Li DD, He YL, Huang JP, Bi L, Ding L (2018) Multiple equilibria in a land-atmosphere coupled system. *J Meteor Res* 32(6):950–973. <https://doi.org/10.1007/s13351-018-8012-y>
- Liu XD, Yanai M (2002) Influence of Eurasian spring snow cover on Asian summer rainfall. *Int J Climatol* 22:1075–1089. <https://doi.org/10.1002/joc.784>
- Mori M, Watanabe M, Shiogama H, Inoue J, Kimoto M (2014) Robust Arctic sea-ice influence on the frequent Eurasian cold winters in past decades. *Nat Geosci* 7:869–873. <https://doi.org/10.1038/ngeo2277>
- Ogi M, Yamazaki K, Tachibana Y (2003) Solar cycle modulation of the seasonal linkage of the North Atlantic Oscillation (NAO). *Geophys Res Lett* 30(22):2170. <https://doi.org/10.1029/2003gl018545>
- Palmer TN, Sun ZB (1985) A modeling and observational study of the relationship between sea surface temperature in the north-west Atlantic and the atmospheric general circulation. *Q J R Meteorol Soc* 111:947–975
- Petoukhov V, Semenov VA (2010) A link between reduced Barents-Kara sea ice and cold winter extremes over northern continents. *J Geophys Res* 115:D21111. <https://doi.org/10.1029/2009jd013568>
- Pyper BJ, Peterman RM (1998) Comparison of methods to account for autocorrelation in correlation analyses of fish data. *Can J Fish Aquat Sci* 55:2127–2140
- Rayner NA, Parker DE, Horton EB, Folland CK, Alexander LV et al (2003) Global analyses of sea surface temperature, sea ice, and night marine air temperature since the late nineteenth century. *J*

- Geophys Res 108:D144407. <https://doi.org/10.1029/2002jd00270>
- Ruzmaikin A, Feynman J (2002) Solar influence on a major mode of atmospheric variability. *J Geophys Res* 107:D144209. <https://doi.org/10.1029/2001jd001239>
- Schwander M, Rohrer M, Brönnimann S, Malik A (2017) Influence of solar variability on the occurrence of central European weather types from 1763 to 2009. *Clim Past* 13:1199–1212. <https://doi.org/10.5194/cp-13-1199-2017>
- Serreze MC, Barrett AP, Stroeve JC, Kindig DN, Holland MM (2009) The emergence of surface-based Arctic amplification. *The Cryosphere* 3:11–19
- Soon W, Legates DR (2013) Solar irradiance modulation of Equator-to-Polar temperature gradients: empirical evidence for climate variability on multi-decadal times. *J Atmos Solar-Terr Phys* 93:45–56
- Steven S (2000) Nonlinear dynamics and chaos: with applications to physics, biology, chemistry and engineering. Perseus Books, New York
- Sun CH, Yang S, Li WJ, Zhang RN, Wu RG (2016) Interannual variations of the dominant modes of East Asian winter monsoon and possible links to Arctic sea ice. *Clim Dyn* 47:481–496. <https://doi.org/10.1007/s00382-015-2851-3>
- Sutton RT, Dong BW, Gregory JM (2007) Land/sea warming ratio in response to climate change: IPCC AR4 model results and comparison with observations. *Geophys Res Lett* 34:L02701. <https://doi.org/10.1029/2006gl028164>
- Takaya K, Nakamura H (2005) Mechanisms of intraseasonal amplification of the cold Siberian high. *J Atmos Sci* 62:4423–4440. <https://doi.org/10.1175/jas3629.1>
- Tan GR, Ren HL, Chen HS, You QL (2017) Detecting primary precursors of January surface air temperature anomalies in China. *J Meteorol Res* 31(6):1096–1108. <https://doi.org/10.1007/s13351-017-7013-6>
- Tao SY (1957) A synoptic and aerological study on a cold wave in the Far East during the period of the break down of the blocking situation over EuroAsia and Atlantic. *Acta Meteorol Sin* 28(1):63–74 (in Chinese)
- Thompson DWJ, Wallace JM (1998) The Arctic Oscillation signature in the wintertime geopotential height and temperature fields. *Geophys Res Lett* 25:1297–1300
- Thompson DWJ, Wallace JM (2000) Annular modes in the extratropical circulation. Part I: Month-to-month variability. *J Clim* 13:1000–1016
- Timoshenko SP, Gere JM (1961) Theory of elastic stability, 2nd edn. McGraw-Hill, New York
- Wang L, Chen W (2014) The East Asian winter monsoon: re-amplification in the mid-2000s. *Chin Sci Bull* 59(4):430–436. <https://doi.org/10.1007/s11434-013-0029-0>
- Wang L, Chen W, Zhou W, Chan JCL, Barriopedro D, Huang RH (2010) Effect of the climate shift around mid 1970s on the relationship between wintertime Ural blocking circulation and East Asian climate. *Int J Climatol* 30:153–158. <https://doi.org/10.1002/joc.1876>
- Weng HY (2012) Impacts of multi-scale solar activity on climate. Part I: atmospheric circulation patterns and climate extremes. *Adv Atmos Sci* 29(4):867–886. <https://doi.org/10.1007/s00337-012-1238-1>
- Wilks DS (2011) Statistical methods in the atmospheric sciences, 3rd edn. Academic Press, New York
- Wu BY, Huang RH, Gao DY (1999) Effects of variation of winter sea-ice area in Kara and Barents seas on East Asia winter monsoon. *Acta Meteorol Sin* 13(2):141–153
- Xu XP, He SP, Li F, Wang HJ (2017) Impact of northern Eurasian snow cover in autumn on the warm Arctic-cold Eurasia pattern during the following January and its linkage to stationary planetary waves. *Clim Dyn* 50:1993–2006. <https://doi.org/10.1007/s00382-017-3732-8>
- Wang L, Lu MM (2017) The East Asian winter monsoon. In: Chang CC et al (eds) The global monsoon system: research and forecast, 3rd edn. World Scientific Publishing Co, Singapore, pp 51–62
- Yao Y, Luo DH, Dai AG, Simmonds I (2017) Increased quasi stationary and persistence of winter Ural blocking and Eurasian extreme cold events in response to Arctic warming. Part I: insights from observational analyses. *J Clim* 30:3549–3568. <https://doi.org/10.1175/jcli-d-16-0261.1>
- Yeh TC, Tao SY, Zhu BZ (1962) Studies on the blocking situation in the Northern Hemisphere in Winter. Science Press, China (in Chinese)
- Yun KS, Seo YW, Ha JK, Lee JY, Kitoh A (2016) The seasonally varying effect of the Tibetan Plateau on Northern Hemispheric blocking frequency and amplitude. *Clim Dyn* 47:2527–2541. <https://doi.org/10.1007/s00382-016-2981-2>
- Zhang RN, Sun CH, Zhang RH, Jia LW, Li WJ (2018) The impact of Arctic sea ice on the inter-annual variations of summer Ural blocking. *Int J Climatol* 38:4632–4650. <https://doi.org/10.1002/joc.5731>
- Zheng QL, Gu Y, Song QL, Jiang P (1993) Numerical study on effects of the Qinghai-Xizang plateau on formation of the Ural Blocking high. *Acta Meteorol Sin* 7(1):61–69

**Publisher's Note** Springer Nature remains neutral with regard to jurisdictional claims in published maps and institutional affiliations.